Title

Extensive monolayer formation depends on a subpopulation of transplanted human iPSC-derived RPE cells

Authors

Karen Tessmer[1], Sylvia J. Gasparini[1,2], Klara Schmidtke[1], Trishla Adhikari[1], Lea Michalke[1], Juliane Hammer[1], Liliana R. Loureiro[3], Annika Last[4], Nadine Chelius[4], Annett Kurtz[4], Hannah Johannsen[4], Madalena Carido[1,5], Susanne Ferguson[1], Andreas Petzold[6], Ulrike A. Friedrich[6], Thomas Kurth[7], Andreas Dahl[6,8], Anja Feldmann[3,9,10], Seba Almedawar[1,2], Sebastian Knöbel[4#], Marius Ader[1#*]

Affiliations

[1] Center for Regenerative Therapies Dresden (CRTD), Center for Molecular and Cellular Bioengineering (CMCB), Technische Universität Dresden (TUD), 01307 Dresden, Germany

[2] Boehringer Ingelheim Pharma GmbH & Co. KG, 88400 Biberach, Germany

[3] Institute of Radiopharmaceutical Cancer Research, Helmholtz-Zentrum Dresden-Rossendorf (HZDR), 01328 Dresden, Germany

[4] Miltenyi Biotec B.V. & Co. KG, 51429 Bergisch Gladbach, Germany

[5] German Center for Neurodegenerative Diseases (DZNE), 01307 Dresden, Germany

[6] DRESDEN-concept Genome Center, Technology Platform at the Center for Molecular and Cellular Bioengineering (CMCB), Technische Universität Dresden (TUD), 01307 Dresden, Germany

[7] Core Facility Electron Microscopy and Histology, Technology Platform at the Center for Molecular and Cellular Bioengineering (CMCB), Technische Universität Dresden (TUD), 01307 Dresden, Germany

[8] German Center for Diabetes Research (DZD e.V.), 85764 Neuherberg, Germany; Paul Langerhans Institute Dresden of the Helmholtz Center Munich, University Hospital and Faculty of Medicine Carl Gustav Carus, Technische Universität Dresden (TUD), 01307 Dresden, Germany

[9] German Cancer Consortium (DKTK), Partner Site Dresden, 01307 Dresden, Germany; German Cancer Research Center (DKFZ), 69120 Heidelberg, Germany

[10] National Center for Tumor Diseases Dresden (NCT/UCC), Partner Site Dresden, 01307 Dresden, Germany

Author list footnotes

[#] equal contribution

Corresponding author e-mail address

* Correspondence: marius.ader@tu-dresden.de

Abstract

Loss of retinal pigment epithelium (RPE) cells in the eye leads to photoreceptor death and vision loss. Cell replacement strategies using RPE derived *in vitro* from pluripotent stem cells (PSCs) has emerged as a promising therapeutic strategy. Generation of polarized monolayers represents an essential prerequisite for proper RPE function, however, monolayer formation following transplantation of RPE cell suspensions has not been systematically assessed. Using the sodium iodate mouse model of RPE depletion, significant increase in monolayer formation capacity of passage (P) 1 vs. P2 human iPSC-derived RPE cells was observed three weeks after transplantation. Transplant-derived monolayers showed characteristic apicobasal polarity, RPE marker expression, phagocytosis function, and preservation of the host outer nuclear layer. The cell surface marker panel $CD54^{+}$/PSA-$NCAM^{-}$ was identified to enrich for an RPE subpopulation with high potential for monolayer formation following transplantation. Results underline the importance of defining and isolating competent cell subpopulations for successful RPE transplantation.

Keywords

cell surface marker / monolayer formation/ retina/ retinal pigment epithelium/ transplantation

Introduction

Deterioration of the retinal pigment epithelium (RPE), an epithelial monolayer separating choroid and neuroretina in the eye, causes retinal degeneration including dysfunction and loss of the light sensitive photoreceptors. Diseases comprising RPE pathologies include subforms of retinitis pigmentosa as well as age related macular degeneration (AMD), the main cause for vision impairment and blindness in industrialized societies (Fleckenstein *et al*, 2021). Loss of RPE cells is considered permanent given limitations of intrinsic regeneration in the mammalian retina, while cell transplantation approaches for the replacement of RPE are discussed as a potential therapeutic approach. Indeed, preclinical and clinical phase I/II studies using human pluripotent stem cell (PSC)-derived RPE cells provide evidence for safety of the approach, long-term survival of donor cells and some signs of vision stabilization or even improvements (Gupta *et al*, 2023).

Two principal delivery approaches, both in most cases targeting the subretinal space, have mainly been used: injection of either an RPE cell suspension or a preformed RPE sheet or patch (i.e. RPE cultured on a scaffold). While sheets or patches have the advantage to resemble an already formed polarized monolayer, their delivery into the diseased eye is associated with major obstacles, requiring sophisticated surgery techniques with increasing danger of ruptures in significantly thinned and gliotic degenerative retinas (Gupta *et al*, 2023). Cell suspensions, on the other hand, are more easily injected into the subretinal space, but still have to form a polarized monolayer on Bruch's membrane in vivo. A recent direct comparison of suspension vs. patch transplantations provided evidence for improved survival and functionality of preformed patches in an acute laser-induced porcine-model of RPE damage (Sharma *et al*, 2019). On the other hand, several clinical RPE replacement trials, with one moving forward to phase 2a, are based on suspension transplantation showing evidence for vision stabilization and improvement in AMD/geographic atrophy patients (Gupta *et al*, 2023).

While PSC-derived RPE cells show significant changes in gene expression profiles and morphology over multiple passages leading eventually to de-differentiation and epithelial-to-mesenchymal transitions (Singh *et al*, 2013), recent single cell transcriptome analysis of stem cell-derived RPE in vitro provided evidence for a high heterogeneity within RPE cells also at low passages (Farjood *et al*, 2023; Petrus-Reurer *et al*, 2022). Interestingly, a subpopulation of RPE cells derived from in vitro expanded RPE stem cells (RPESCs) showed improved transplantation efficacy in the pre-clinical RCS rat model when used from an early passage (Davis *et al*, 2017) and an RPE subpopulation expressing the lncRNA TREX displayed improved integration capacity in an existing RPE monolayer in vitro (Farjood *et al*, 2023). However, a systematic and quantitative analysis for the competence of specific PSC-derived RPE subpopulations for monolayer formation in vivo has not been performed yet.

Using the sodium iodate ($NaIO_3$) RPE depletion mouse model as recipient (Anderson *et al*, 2024; Carido *et al*, 2014), we provide evidence that iPSC-RPE isolated from passage 1 generate extensive polarized RPE monolayers within three weeks after suspension transplantation covering up to 35% of the host retinal surface with protection of the outer nuclear layer (ONL) structure. Contrarily, passage 2 RPE cells showed a reduced coverage in recipient mouse retinas, and their capacity to form polarized monolayers was significantly decreased, resulting in a disrupted ONL, choroid swelling and increased infiltration of immunogenic cells. Interestingly, enriching for a passage 1 RPE subpopulation that can be isolated by cell surface epitope sorting ($CD54^+$/PSA-$NCAM^-$) consistently results in higher monolayer percentages than usage of unsorted passage 1 RPE cells (up to 80% of transplant area). Our findings thus underline the importance of defining and isolating competent RPE subpopulations for successful RPE transplantation approaches.

Results

While morphologically similar, expression profiles of human iPSC-derived RPE differ after passaging

RPE cells were generated by differentiation of iPSC with initial epithelial cyst formation in Matrigel followed by polarized monolayer formation on cell culture inlets and repeated passaging (Fig. 1A) (Almedawar *et al*, 2020; Schreiter *et al*, 2020; Zhu *et al*, 2013). Both, passage (P) 1 and P2 RPE cells acquired pigmentation and a cobblestone-like morphology, with zonula occludens 1 (ZO1)-positive tight junctions and actin enrichment at the apical surface (Figs. 1B and C). Proper polarization was further evident in the cross-sectional view by basal and apical positioning of nuclei and pigment granules, respectively, as well as basal deposition of collagenIV (COL4), and apical enrichment of sodium/potassium-transporting ATPase (ATP1A1) and F-actin (Fig. 1C). Ultrastructural analysis confirmed the apicobasal polarization of the cells with basally located nucleus, basal labyrinth and mitochondria, apically located microvilli and melanosomes, and connections via tight and adherens junctions (Fig. 1D).

Transcriptome analysis of P1 and P2 RPE populations by bulk RNA sequencing revealed close clustering of cells from the same passage across batches in principle component analysis (Fig. 1E). However, both P1 and P2 cells exhibited high expression levels of typical RPE genes characteristic for the visual cycle (e.g. BEST1, SFRP5, RLBP1), phagocytosis (e.g. LAMP2, ERMN, GULP1), or pigmentation (e.g. DCT, PMEL, MITF) and others (Fig. 1F

103 and Doc. S2 sheet 1). Differential gene expression analysis returned a higher number of genes up-regulated in
104 P1 cultures than in P2 (P1: 853, P2: 229, Doc. S2 sheets 2 and 5), possibly caused by a lower overall RPE purity
105 or due to the developmentally younger P1 RPE not yet being as transcriptomically defined. Indeed, genes more
106 highly expressed in P1 cells were overrepresented in GO terms related to neuronal and muscular cell identity
107 and function as well as transcriptional processes (Figs. 1G and I, Doc. S2 sheets 3 and 4), suggesting the presence
108 of non-RPE cells or young P1 RPE cells at a more pliable stage. In P2 cultures, the upregulated genes were
109 overrepresented in GO terms related to the extracellular matrix and immune-related processes (Figs. 1H and J,
110 Doc. S2 sheets 6 and 7).

111 In summary, while morphologically similar and showing RPE characteristics, P1 and P2 iPSC-RPE cultures
112 also displayed significant differences in their expression profiles possibly affecting downstream applications.
113

114 Single cell suspension transplantation of P1 but not P2 RPE yields large areas of 115 polarized RPE monolayer

116 Using the $NaIO_3$ mouse model of RPE degeneration as recipient (Carido *et al*, 2014), the potential of
117 transplanted P1 and P2 iPSC-RPE cells for survival and monolayer formation was assessed. To that end, adult
118 wild type mice (C57BL/6j) received a tail vein injection of 30 mg/kg $NaIO_3$ which was sufficient to result in RPE
119 depletion, disruption of the choroid-retina barrier as shown by retinal angiography, photoreceptor death as
120 measured by TUNEL assay and function loss as measured by ERG within 3-7 days (Fig. S1). Seven days after $NaIO_3$
121 injection, P1 or P2 RPE cell suspensions were transplanted into the subretinal space of hosts (Fig. 2A).

122 Three weeks after transplantation immunohistochemical analysis showed the presence of both P1 and
123 P2 cells in the subretinal space (Figs. 2B and C). Retinal cryosections provided further insights into the
124 distribution and organization of transplanted donor cells: While human P1 cells appeared to mainly form single-
125 cell monolayers and only few cell clusters (Fig. 2B-B''), P2 cells appeared to generate mainly cell clusters and
126 only few monolayer-like structures (Figs. 2C and C'). Generally, RPE monolayers showed typical characteristics
127 of apicobasal polarization including apical expression of ATPase and F-actin besides apical accumulation of
128 pigment granules, as well as a basally located nucleus and basal expression of collagen IV (Fig. 2D). In contrast,
129 clusters of donor cells showed few signs of polarized expression of these apical and basal markers, which were
130 rather found distributed chaotically throughout the graft (Fig. 2D). The differences between cell monolayers and
131 clusters in regard to cell organization and polarization were confirmed by ultrastructural analysis (Fig. 2E). Here,
132 cells within monolayers showed a polarized distribution of RPE organelles, with melanosomes located apically,
133 while the nucleus, basal labyrinth and mitochondria were located basally (Figs. 2E and S2A-A'''). Clustered cells,
134 in contrast, had a chaotic appearance without obvious signs of polarization and instead often contained large
135 quantities of pigment granules (Fig. 2E). Additionally, laterally located adherens and tight junctions were
136 regularly observed between cells organized in a monolayer, but missing in cell clusters (Figs. 2E, S2A'' and S2A''').

137 Quantification of whole retina serial sections by fluorescence microscopy revealed that P1 cells
138 occupied almost double the retinal surface as P2 cells (P1: 27.6%±1.6, P2: 14.8%±1.7, Fig. 2F). Additionally, while

139 the majority of human P1 RPE occupied area presented as a monolayer (78.8%±2.7), only 19.4%±3.8 of the P2
140 RPE area adopted monolayer conformation, with the majority of cells instead forming clusters (Fig. 2G).
141 Figs. 2F and 2G both contain data from transplanting either 50,000 or 100,000 cells per eye, as
142 aggregating the data by cell number transplanted revealed similar coverage and monolayer formation rates in
143 both cases (Fig. S2B). While not statistically significant, transplanting the lower cell number even led to a slightly
144 increased monolayer formation (Fig. S2B), thus for all further transplantations shown here 50,000 cells/retina
145 were used. Additionally, analysis at 1, 2, or 3 weeks after P1 RPE transplantation revealed a continuous increase
146 in the proportion of monolayer area (week 1: 44.0%, week 2: 63.4%, week 3: 80.9%, Fig. S2C).
147 In summary, while human P1 and P2 RPE both survived for up to 3 weeks after transplantation in mouse
148 RPE depleted recipients, P1 cells formed significantly larger areas of polarized, single cell monolayers than P2
149 cells, which instead mainly generated cell clusters.
150

151 Human RPE monolayers preserve ONL organization and phagocytose outer 152 segments

153 Proper RPE structure and function is required for photoreceptor homeostasis and light detection.
154 Under homeostatic conditions, photoreceptor organization is characterized by tight stacking of cell
155 bodies/nuclei in the ONL and the presence of a continuous, straight outer limiting membrane (OLM). Irregular
156 stacking and an interrupted, strongly curved OLM indicate that the photoreceptors are stressed or damaged.
157 Thus, as a proxy of photoreceptor support by RPE, we quantified the presence of 'organized' vs. 'disorganized'
158 ONL areas, as shown by the OLM either being parallel or not parallel to the INL (Fig. 2H). Indeed, quantification
159 revealed a strong photoreceptor support by RPE monolayers, as 88.8 ± 5.4 % of ONL beneath RPE monolayers
160 retained an organized shape (Fig. 2I). In contrast, below cell clusters of either P1 or P2 RPE cells, only 5.7 ± 9.5
161 % of ONL appeared organized, with the majority of the ONL instead generating foldings, tubulations, rosettes,
162 and exhibiting dislocated nuclei (Fig. 2I). This phenotype was even more pronounced than in areas without any
163 RPE cells, where 27.2 ± 2.7 % of ONL area remained organized (Fig. 2I, compare also Figs. 2B-B''', C-C''). These
164 results highlight the notion that formation of a proper RPE monolayer is essential to support ONL preservation.
165 Another key RPE function is the continuous phagocytosis of shed outer segments. Phagosomes
166 containing mouse outer segments can be found in the vicinity of human RPE monolayer nuclei in wild type $NaIO_3$-
167 treated animals (Fig. S3A). To further validate the capacity of transplanted human RPE to phagocytose mouse
168 outer segments, P1 RPE cells were transplanted into $NaIO_3$-treated rhoEGFP mice, which express a Rhodopsin-
169 EGFP fusion protein that localizes to outer segments (Chan *et al*, 2004). Immunofluorescent staining (Figs. 3A
170 and A') and ultrastructural analysis by correlative light and electron microscopy (CLEM) at 3 weeks post
171 transplantation confirmed the presence of GFP-positive structures within the human RPE cells, indicating their
172 phagocytotic activity (Figs. 3B-B'' and C-C'').
173

174 ## P2, but not P1 RPE transplants induce a strong immunological response

175 In healthy conditions, the retina represents an immune-privileged tissue, with resident microglia and
176 Müller Glia (MG). Upon $NaIO_3$-induced RPE and photoreceptor loss, MG become gliotic and GFAP upregulation
177 was present in both P1- and P2- transplanted eyes (Fig. S3B). However, striking differences in choroid thickness
178 and microglia activation were observed between P1 and P2 transplanted retinas. The choroid of eyes
179 transplanted with P2 RPE cells was on average more than twice as thick compared to eyes transplanted with P1
180 RPE (53.7 ± 19.7 µm and 23.0 ± 9.3 µm respectively; Fig. 3D). Additionally, in P2 RPE-transplanted retinas a
181 striking increase of cells positive for IBA1 (Ionized calcium-binding adapter molecule 1), a marker for microglia
182 and macrophages, was observed both in the retina and the choroid (Fig. 3F). In P1 RPE transplanted eyes only
183 few $IBA1^+$ cells were located within the retina, mainly in the inner and outer plexiform layers, and almost no
184 $IBA1^+$ cells localized within the choroid (Fig. 3E).

185 In summary, transplantation of P2 RPE cell suspensions triggered a stronger immune reaction in
186 comparison to P1 RPE cells.

187

188 ## Identification of a P1 RPE subpopulation

189 Although in vitro differentiation of RPE is generally considered to yield a homogenous cell product, it
190 has become more and more clear that differences between RPE subgroups exist both in vivo and in vitro, with
191 the latter having important implications in cell performance after transplantation (Farjood *et al*, 2023; Ortolan
192 *et al*, 2022). Obvious phenotypic heterogeneity between cells, namely varying degrees of pigmentation between
193 cells of the same passage P1 (Fig. 1B), inspired an empirical flow cytometry-based screening approach using a
194 pre-formatted antibody panel covering 371 cell surface markers, with the aim to identify markers correlating
195 with subpopulations of differentially pigmented cells. Side scatter signal intensity (SSC) was used as proxy for
196 pigmentation and hits were selected based on either negative or positive correlation to identify depletion or
197 enrichment of marker candidates, respectively (Fig. 4A, Doc. S3). Nine isotype controls and one empty well per
198 screening plate served as controls.

199 After validation of several initial hits the combination of CD54 (ICAM) positivity and PSA-NCAM
200 negativity proved to be the most robust combination allowing identification (Figs. 4B and 4C) and reproducible
201 isolation of highly pigmented target cells (Fig. 4D). Consequently, effective depletion of unpigmented cells and
202 a high degree of pigmentation was observed for the target-enriched (ENR) fraction after replating in vitro (Fig.
203 4D, ENR), while the unsorted and target-reduced fractions showed a lower overall pigmentation level (Fig. 4D,
204 UNS & RED). An average purity of 96.0% $ICAM^+$/$PSA\text{-}NCAM^-$ (Fig. 4E) was achieved in the ENR fraction from cell
205 preparations used in the screening process, which were shipped frozen and stained immediately after thawing.
206 Similarly, fresh cells collected from the transwell inserts directly before staining could be enriched to an average
207 purity of 97.7%, $ICAM^+$/$PSA\text{-}NCAM^-$ (Fig. 4E), the latter being used for subsequent in vivo studies.

208

209 ## Transplanted CD54$^+$/PSA-NCAM$^-$ P1 RPE cells show improved monolayer
210 formation

211 To assess whether the highly pigmented cell surface marker-defined P1 RPE subpopulation has the
212 capacity for monolayer formation after transplantation in vivo, P1 RPE cells were dissociated and sorted using
213 the MACSQuant® Tyto® cell sorter (Miltenyi Biotec) to obtain two cell fractions: CD54$^+$/PSA-NCAM$^-$ enriched
214 (ENR), and CD54$^+$/PSA-NCAM$^-$ reduced (RED) in addition to the unsorted (UNS) control. While the percentage of
215 CD54$^+$/PSA-NCAM$^-$ cells fluctuated in the UNS and RED fraction depending on the differentiation round, sorting
216 consistently yielded >96% pure CD54$^+$/PSA-NCAM$^-$ cells in the ENR fraction (Figs. 4E, S4A and S4B). All cell
217 fractions were subretinally transplanted into the $NaIO_3$ mouse model of RPE depletion and analyzed after three
218 weeks.

219 Immunostaining of human nuclei and F-actin showed large grafts in flat-mounted experimental eyes
220 (Fig. 5A (UNS), B (ENR), C (RED), dashed white outlines). Two main appearances could be distinguished: firstly,
221 graft regions with an intense human nuclei signal but lacking cobblestone morphology, dotted with pigment-
222 rich spheres (Figs. 5A and 5C, magnified in Fig. 5A') likely representing macrophages (Fig. S5A); secondly graft
223 regions exhibiting extensive cobblestone morphology but a seemingly weaker human nuclei signal (Figs. 5B, 5B'
224 and 5B''). It is important to note that this comparatively weak human nuclei staining arises from concealment
225 of the nuclei by the more apically positioned, light-absorbing pigment granules (Figs. S4C-F') in the highly
226 structured and polarized human RPE monolayer. Towards graft edges, the monolayer regions showed again
227 higher human nuclei visibility (Fig. 5B'' and Figs. S4C-F'), suggesting an absence of the characteristic pigment,
228 while neither cobblestone morphology nor human nuclei staining was found outside of the graft areas (Fig. 5C').

229 Exploratory assessment with the image-analysis tool REShAPE (Ortolan *et al*, 2022) allowed the
230 reconstruction and analysis of the graft monolayer regions of one flatmount per fraction (Figs. 5D and S4G-I).
231 REShAPE analysis showed the ENR sample contained 5x and 5.4x as many monolayer cells as the UNS and RED
232 samples, respectively (UNS: 7453, ENR: 37607, RED: 6921 cells; Fig. 5E), and overall generated the largest
233 monolayer cells (mean areas: UNS 57 μm^2, ENR 79 μm^2, RED 55 μm^2; Fig. 5F). The notion of proper RPE
234 monolayer formation by the human cells was further underlined by high numbers of monolayer cells in all
235 fractions neighboring 5 to 7 others, with ENR monolayer cells having the largest number of such cells (UNS: 67%,
236 ENR: 82%, RED: 69%; Fig. 5G)

237 Analysis of retinal cryosections showed human cells again creating polarized single cell monolayers or
238 unorganized clusters between the ONL and the choroid (Figs. 5H and S5B). Interestingly, P1 RPE fractions
239 enriched for CD54$^+$/PSA-NCAM$^-$ cells showed a significantly increased monolayer formation when compared
240 with unsorted cells or cells with a reduced proportion of CD54$^+$/PSA-NCAM$^-$ cells (Fig. 5I), despite similar overall
241 retinal coverage (Fig. S5C). Importantly, enrichment of CD54$^+$/PSA-NCAM$^-$ cells yielded populations with similarly
242 high monolayer formation capacity across experiments (Figs. 5I and 5J). The UNS and RED fractions on the other
243 hand were found to differ strongly in that regard, with cell culture batches that contained a higher percentage
244 of CD54$^+$/PSA-NCAM$^-$ cells yielding more monolayer (Fig. 5I: UNS 72.7% CD54$^+$/PSA-NCAM$^-$ cells) than batches
245 with a lower percentage of CD54$^+$/PSA-NCAM$^-$ cells (Fig. 5J: 34.1% CD54$^+$/PSA-NCAM$^-$ cells).

To test whether enriching CD54$^+$/PSA-NCAM$^-$ cells robustly improves monolayer formation capacity across contexts, we varied sorting strategies. Similarly to the Tyto sorting, enrichment by conventional flow cytometry with a BD FACSAria™ III (BD Bioscience) yielded a purity of >97% in the ENR fraction (Fig. S5D), with the ENR fraction again showing an improved amount of monolayer formation after transplantation into the $NaIO_3$ mouse model compared to cell fractions that were unsorted or reduced in CD54$^+$/PSA-NCAM$^-$ cells (Fig. 5K).

In summary, our combined results provide evidence that an RPE subpopulation sortable by the cell surface markers CD54$^+$/PSA-NCAM$^-$ at an early differentiation stage has the potential for extensive monolayer formation after subretinal transplantation into a mouse model of RPE depletion.

Discussion

While not yet clinically established, transplantation of pluripotent stem cell-derived RPE cells for replacement approaches in the retina have continuously developed over the last two decades, with a number of clinical trials providing evidence for its safety and, in part, showing therapeutic effects like stabilization or even some improvement of visual functions (Gupta *et al*, 2023; Klymenko *et al*, 2024). Advancing RPE cell generation and selection might be helpful to further improve transplantation outcomes. Here, we used the $NaIO_3$ mouse model of RPE depletion to systematically assess the capacity of PSC-derived RPE cells to form polarized monolayers after transplantation in vivo. Our combined results provide evidence that human P1 RPE cells have a significantly increased potential in comparison to P2 RPE cells to generate extensive monolayers with rescue properties in the mouse retina. Additionally, cell surface marker sorting by CD54$^+$/PSA-NCAM$^-$ allowed isolation of a monolayer-forming subpopulation within the P1 RPE cell population, independent of the sorting method used. Thus, defining competent RPE cells appears as an important precondition to improve transplantation outcomes.

Polarized monolayer formation is an essential prerequisite for RPE cells to properly function. The RPE monolayer is part of the retina-blood-barrier in the eye and is involved e.g. in the phagocytosis of photoreceptor outer segments, ion buffering, epithelial transport of nutrients, ions and water, growth factor secretion, and light absorption (Strauss, 2005). We saw striking differences in the potential of RPE cells at different developmental stages to generate monolayers after transplantation into a retinopathy mouse model depleted of endogenous RPE. While “young” RPE cells, i.e. P1 cells, generated extensive monolayers, P2 RPE cells instead mainly generated unorganized cell clusters. Immunohistochemical and ultrastructural analysis revealed a mature RPE phenotype within donor cell-derived monolayers including apicobasal polarized location of diverse organelles and proteins, which was absent in donor cells organized in clusters. The formation of RPE monolayers consequently had a significant influence on the underlying ONL: while underneath cell clusters the ONL showed massive pathological changes including foldings, tubulations and photoreceptor loss, as it was also observed in areas without RPE cells, the ONL in regions with newly formed RPE monolayers did not show signs of degeneration and had a highly organized appearance. Thus, the formation of monolayers appears to be essential for these therapeutic effects. Indeed, a recent study using RPE derived from RPESCs showed improved ONL and vision function rescue after transplantation at an early, defined developmental stage into the RCS model of RPE

283 dysfunction (Davis *et al*, 2017). However, whether improved monolayer formation or other factors were the
284 underlying mechanism for the described rescue effects was not assessed in that study (Davis *et al*, 2017).
285 In order for cell transplantations to be successful, the heterogeneity of RPE in vivo and in RPE cultures
286 should be taken into account. Distinct RPE subpopulations were recently identified within concentric regions of
287 the adult human retina, calling for further characterization and selection of RPE subpopulations in regard to
288 function and potential therapeutic use in central versus peripheral retinal regions (Ortolan *et al*, 2022). Similarly,
289 single cell RNAseq analysis of primary and stem cell-derived RPE populations revealed a higher heterogeneity,
290 also in early passages in culture, than previously thought (Farjood *et al*, 2023; Petrus-Reurer *et al*, 2022; Plaza
291 Reyes *et al*, 2020; Voigt *et al*, 2019; Xu *et al*, 2021). Thus, also subpopulations of cultured RPE cells must be
292 characterized more thoroughly with regards to their potential for integration and monolayer formation after
293 transplantation in vivo. Interestingly, expression profiling in our study also showed significant differences in gene
294 expression already at early passages, i.e. between P1 and P2 RPE cultures, though the morphological appearance
295 including monolayer formation, pigmentation, and RPE-specific marker expression in vitro was still similar.
296 Given the high possible heterogeneity within and between cell culture batches, it is vital to understand
297 the effect of cell subpopulations on transplantation outcomes when moving forward with clinical trials. Cell
298 surface marker-based sorting therefore represents an important tool for high-throughput target cell isolation
299 and quality control in a donor cell production pipeline. For stem cell-derived RPE cultures several studies
300 identified RPE-specific cell surface markers, mainly with the goal to purify RPE cells from heterogenous cultures,
301 particularly for protocols that were previously based on manual separation of pigmented cell populations (Plaza
302 Reyes *et al*, 2020; Sharma *et al*, 2022). As such, removal of unwanted, non-RPE cells using $CD56^+$ and $CD24^+$ cell
303 depletion has been introduced for the generation of RPE monolayers and patches in vitro for transplantation
304 purposes (Sharma *et al*, 2022). Reyes et al identified $CD140b^+/CD184^-$ sorting for improving RPE cultures that
305 also have the capacity for monolayer formation after transplantation in rabbits (Plaza Reyes *et al*, 2020), while
306 the lncRNA TREX has been identified as a biomarker for RPESC-derived RPE with increased monolayer forming
307 capacity in vitro and potential for functional improvement after transplantation into RCS rats (Farjood *et al*,
308 2023). It would be of great interest to systematically and quantitatively assess these markers or their
309 combinations in regard to RPE monolayer formation after transplantation in vivo.
310 Our human cell surface marker screen using 371 cell surface antibodies identified multiple cell surface
311 markers capable of selecting highly pigmented RPE subpopulations. This screening data is a valuable resource
312 for future refinement of sorting strategies confirming on the one hand the validity of already reported markers
313 (CD24, CD56) and suggesting additional candidates (e.g. CD44, CD239; see also Doc. S3). In our hands, however,
314 the marker combination $CD54^+$/PSA-$NCAM^-$ proved to be most robust during validation and indeed allowed to
315 isolate a key RPE subpopulation contributing to monolayer formation after transplantation into the RPE-
316 depleted $NaIO_3$ mouse model. Direct quantitative comparison of $CD54^+$/PSA-$NCAM^-$ enriched (>95%) vs reduced
317 (<50%) RPE fractions showed significant differences in monolayer formation in vivo. While the identification of
318 potential cell surface markers for the enrichment of specific RPE subpopulations was based on pigmentation
319 intensity, a recent study provided evidence that pigmentation intensity by itself does not correlate with specific

320 RPE marker expression (Nakai-Futatsugi *et al*, 2024). Thus, further studies might be necessary to assess in more
321 detail the direct (or indirect) context between pigmentation intensity and RPE maturation.
322 Indeed, the marker combination CD54$^+$/PSA-NCAM$^-$ might also mechanistically reflect its use for
323 homogenous RPE monolayer formation as CD54 represents the intercellular adhesion molecule 1 (ICAM-1), an
324 adhesion molecule of the immunoglobulin superfamily, classically involved in intercellular adhesion. The epitope
325 PSA-NCAM, derived from the posttranslational modification of the neural cell adhesion molecule (NCAM) with
326 polysialic acid, is considered a marker for immature neural precursors (Nguyen *et al*, 2003) and can be used to
327 isolate primitive, proliferative neural progenitors derived from pluripotent stem cells (Barral *et al*, 2013; Kim *et*
328 *al*, 2012). Thus, depletion of PSA-NCAM$^+$ cells may reduce undesirable contaminants with proliferative potential
329 and fate. The combinatorial approach with a positive marker confers a double layer of security to reduce
330 heterogeneity of RPE cell compositions since an independent positive criterion may discriminate unpredictable
331 off-target fates. Furthermore, the purification process allows for seamless implementation into GMP-
332 manufacturing, e.g. based on MACS technology or GMP-compliant multiparametric cell sorting in a closed
333 cartridge system using MACSQuant Tyto cell sorter.
334 When characterizing the human RPE grafts, the REShAPE artificial intelligence-based image analysis tool
335 (Ortolan *et al*, 2022) allowed the assessment of entire human RPE transplant monolayers with single-cell
336 resolution. Indeed, the donor cell-derived monolayers in the $NaIO_3$ mouse model were highly similar in
337 morphology, shape and number of neighboring cells to RPE monolayers in the human eye. While the average
338 size of human RPE after transplantation in the mouse was significantly smaller than in adult human eyes (here:
339 60-80 µm^2, (Ortolan *et al*, 2022) between 150 – 350 µm^{2,}), the smaller size might be a result of the developmental
340 stage of the iPSC-RPE used (P1) and time after transplantation (3 weeks), thus still representing fetal RPE cells
341 rather than the far older RPE cells of donor ages 56-92 years described by Ortolan et al Further increasing the
342 time of donor RPE in vivo would therefore be interesting to study. Additionally, specific signals or mechanic
343 restrictions coming from the mouse environment might influence the growth of transplanted human RPE cells.
344 Currently, RPE replacement clinical trials either inject cell suspensions or preformed monolayers as
345 sheets or on scaffolds as patches (Gupta *et al*, 2023; Klymenko *et al*, 2024). An obvious advantage of
346 sheets/patches is the already formed monolayer allowing for immediate activity and reduction of disorganized
347 cell fractions. However, their placement underneath the retina, particularly in a degenerative environment, is
348 associated with challenging surgery, while the subretinal application of a cell suspension is less traumatic.
349 Interestingly, both delivery approaches appear to be safe and reproducible showing long-term survival with
350 limited immune responses in some patients for more than three years (Gupta *et al*, 2023; Klymenko *et al*, 2024).
351 Sharma et al directly compared RPE suspension and patch injections in the RCS rat model of RPE dysfunction,
352 showing similar ONL and functional rescue potential for both delivery methods, though the patch contained only
353 10,000 while the suspension contained 100,000 cells (Sharma *et al*, 2019). However, the histological images in
354 that study showed that the RPE suspensions formed only unorganized cell clusters and no monolayers in the
355 recipients, suggesting that effects other than specific RPE function might be responsible for the observed
356 histological and functional improvements: a well described phenomenon in RCS rats, where the injection of
357 diverse cell populations including e.g. neural progenitors, fibroblasts, or Schwann cells resulted in rescue effects

358 (Lawrence *et al*, 2000; Wang *et al*, 2008; Zhu *et al*, 2013). In contrast, after injection into a laser-induced retinal
359 degeneration porcine model, the RPE patches showed increased rescue potential in comparison to RPE
360 suspensions at the tissue as well as functional level (Sharma *et al*, 2019). Again, cell suspensions in that study
361 did not generate single-cell monolayers but instead formed unorganized cell clusters that lost expression of the
362 RPE maturity marker RPE65. Whether the poor performance of transplanted RPE suspensions in the porcine
363 model was caused by not selecting for the proper RPE sub-population prior to injection or the animal model
364 chosen would be interesting to assess. Indeed, specific environmental requirements, like a still remaining
365 Bruch's membrane, might be advantageous for proper monolayer formation after RPE suspension injections
366 (Gullapalli *et al*, 2005). This possibility not only calls for the systematic assessment of different RPE degeneration
367 models to test RPE replacement strategies but also emphasizes the need to refine the selection of patients,
368 disease forms and disease stages to identify suitable environments for successful transplantation approaches in
369 clinical trials.

370 In conclusion, the developmental stage/differentiation time of in vitro generated RPE cells significantly
371 influences their monolayer formation capacity after transplantation in vivo. Furthermore, the cell surface
372 markers $CD54^+$/PSA-$NCAM^-$ allow for enrichment of a monolayer-forming RPE subpopulation, highlighting the
373 need for the careful selection of appropriate donor cells for cell replacement approaches of RPE in the eye.
374 These insights might be helpful for improving success of RPE suspension transplantation also in future clinical
375 applications.

376 Methods

377 REAGENTS AND TOOLS TABLE

REAGENT OR RESOURCE	SOURCE	IDENTIFIER
Experimental Models		
iPS cells: CRTD1	CRTD	https://hpscreg.eu/cell-line/CRTDi004-A RRID:CVCL_YR23
iPS cells: MILi001-A	Miltenyi Biotec	https://hpscreg.eu/cell-line/MILi001-A RRID:CVCL_A8MM
Mice: C57BL/6JRj (*M. musculus*)	Janvier	C57BL/6JRj
Mice: rhoEGFP (*M. musculus*)	John H. Wilson, Baylor College of Medicine, Houston, TX 77030	(Chan *et al*, 2004), $Rho^{tm3(RHO/GFP)Jhw}$
Antibodies		
anti-ZO1 (rabbit polyclonal)	Invitrogen	61-7300, RRID:AB_2533938
anti-COL4 (rabbit polyclonal)	Abcam	ab6586, RRID:AB_305584
ATPase (rabbit monoclonal, clone EP1845Y)	Abcam	ab76020, RRID:AB_1310695

Human Nuclei: Anti-HuNu (mouse monoclonal, clone 235-1)	Merck Millipore	MAB1281, RRID:AB_94090
Human Nuclei: KU80 (rabbit monoclonal, clone C48E7)	Cell Signaling	2180, RRID:AB_2218736
Human Nuclei: Stem101 (mouse monoclonal)	Takara	Y40400, RRID:AB_2895096
IBA1 (rabbit polyclonal)	WAKO	019-19741, RRID:AB_839504
CD54-APC (recombinant human, clone REA266)	Miltenyi Biotec	130-121-342, RRID:AB_2784251
PSA-NCAM-PE (mouse monoclonal, clone 2-2B)	Miltenyi Biotec	130-117-394, RRID:AB_2727931
Chemicals, Enzymes and other reagents		
Phalloidin-iFluor 647	abcam	ab176759
Software		
Fiji v2.3.0/1.53q	(Schindelin *et al*, 2012)	https://imagej.net/software/fiji/
RStudio v 2024.04.0+735	Posit PBC	https://posit.co/
MACSQuantify™ v2.13.0, v2.13.3	Miltenyi Biotec	https://www.miltenyibiotec.com/US-en/products/macsquantify-software.html#130-094-559
REShAPE v1.0.4	(Ortolan *et al*, 2022)	https://github.com/nih-nei/REShAPE
Affinity™ Designer v1.10.4	Serif Europe	https://affinity.serif.com/de/designer/

Methods and Protocols

Animals

Details and sources of mouse lines can be found in the Key Resources table. Animals were maintained on a standard 12 hour light-dark cycle. Mice were provided with fresh bedding and nesting weekly and received food and water ad lib. One week before transplantation, endogenous RPE was ablated by a systemic injection of 30 mg/kg body weight sodium iodate ($NaIO_3$) in isotonic NaCl solution into the tail vein. Animals were used for transplantation 7 days later, at 9-13 weeks of age, and kept for a further 3 weeks post-transplantation, under the conditions described above. Only females were used as recipients. Animals received treatment in both eyes, consisting of a subretinal injection of the cell suspension, followed by intravitreal injection of an immune suppressant (details below). No systemic immunosuppression was administered. Animals were sacrificed by cervical dislocation. All animal experiments adhered to the ARVO Statement for the Use of Animals in Ophthalmic and Vision Research and were approved by the animal ethics committee of the TU Dresden and the Landesdirektion Dresden (DD24.1-51531/449/69).

Cell lines

Cell line details can be found in the Key Resources table. CRTD1 cells were cultured at 37°C, 5% CO_2, in mTeSR PLUS (StemCell Technologies, 100-0276) on plates coated with Matrigel hESC-qualified matrix (Corning, 354277) with medium changes every 2-3 days. Colonies were passaged as aggregates using Dispase (StemCell Technologies, 07923) when reaching 40-60% confluency (every 3-7 days, depending on growth speed).

Animal model characterization

Quantification of RPE cell number and cell death

To characterize the animal model, RPE cell number was quantified by counting the number of RPE cells present within a distance of 200 µm around the optic nerve in cross sections where the optic nerve head (ONH) was present (7-24 sections per animal), including only cells with a wild type morphology and/or visible DAPI staining. To evaluate cell death, slides were submitted to the TUNEL assay (Roche, 11684795910), according to the manufacturer's instructions, and the total of TUNEL-positive cells per section was counted in four sections per animal where the ONH was present.

Electroretinogram (ERG)

Mice were dark-adapted overnight and anesthetized under dim red light by an intraperitoneal injection of 30 µg/kg bodyweight (bw) Ketamine (medistar, 04-03-9264/23) and 1 µg/kg bw Medetomidine hydrocholoride (Orion Pharma, Domitor®) in sterile isotonic solution (Fresenius Kabi, B306175/03), followed by application of dilating eye drops containing 2.5% phenylephrine and 0.5% tropicamide (University Clinic Pharmacy Dresden). After 1-2 min, eye drops were replaced with clear moisturizing eye gel (Bausch+Lomb, Vidisic). Full-field ERGs were recorded using a Ganzfeld bowl (Roland Consult). Single-flash responses were obtained under dark-adapted (scotopic, with the following intensities: 0.0003, 0.001, 0.003, 0.01, 0.03. 0.1, 0.3, 1, 3 and 10 cd.s.m-2) and light-adapted (photopic, 10 cd.s.m-2) conditions. Light adaptation was achieved with a background illumination of 30 cd/m^2 starting ten minutes before photopic recordings. Five responses were averaged with inter-stimuli interval of five (0.0003-0.3 cd.s.m-2) or 17 seconds (1-10 cd.s.m-2). For reversal of the anesthesia, animals were intraperitoneally injected with 10 mg/kg bw atipamezole hydrochloride (Orion Pharma, Antisedan®), placed in a warmed cage and monitored until fully awake.

Fundus imaging and Fluorescein angiography

Fundus images were taken with a Phoenix MICRON® IV after animal anesthesia, pupil dilation and eye moisturizing as described above. For fluorescein angiography, animals were recorded 10-15 min after intraperitoneal injection of 10 µl/g bw 1% fluorescein (Alcon, H12588-0113, diluted in isotonic solution). Anesthesia was reversed as described above.

Differentiation of RPE cells

Cyst generation

RPE cells were differentiated as described and patented in (Tanaka & Zhu, 2015; Zhu *et al*, 2013, 2016; Zhu & Tanaka, 2016). Briefly, after removal of undifferentiated colonies, cells were washed twice with warm DMEM/F12 (Gibco, 31330-038) and incubated with Dispase for 7 min at 37°C. The Dispase was gently washed away twice with warm DMEM/F12, then warm N2B27 medium was added and the colonies scraped into a 15 ml

429 Falcon tube, then centrifuged for 1 min at 92 g, room temperature (RT). The pellet containing roughly 50-100
430 µm large cell aggregates was resuspended in N2B27 medium (DMEM/F12+GlutaMAX (Gibco, 31331-028) and
431 neurobasal medium (Gibco) at a 1:1 ratio, 0.5% GlutaMAX Supplement (Gibco, 35050061), 0.5x B-27 supplement
432 (Gibco, 17504044), 0.5x N-2 supplement (Gibco, 17502048), 0.1 mM β-mercaptoethanol (Gibco, 11528926), 1x
433 Penicillin-Streptomycin (Gibco, 15140-122)), placed on ice and gently mixed 2-3 times with cyst Matrigel
434 (Corning, 354234; protein concentration 9-10 mg/ml) using P1000 wide bore tips. Per 1 mm pellet height, 20 µl
435 N2B27 medium and 200 µl Matrigel were used. 100 µl cyst Matrigel with cells were then transferred to a glass
436 bottom dish (Mattek, P35G-1.5-14-C), spreading the mix over the majority of the glass area and allowing the
437 matrix to gel for 10 min at 37°C, the first 5 min upright, the second 5 min inverted. Then, N2B27 medium was
438 added and exchanged every two days.

439 *Plating*

440 To release the cysts formed by day (D) 5 (embedding is counted as D0), 5 Matrigel drops were
441 transferred to 1 ml cold Cell Recovery Solution (BD Biosciences, 354253) in a 15 ml Falcon, incubated on ice for
442 25 min with careful inversion every 2 min. After allowing the cysts to sink for 5 min, removal of the Cell Recovery
443 Solution, a wash with PBS and 1 min centrifugation at 17 g, RT, the pellet was resuspended using a wide bore
444 P1000 tip in TrypLE (GIBCO, 12563-011) diluted 1:6 in PBS. After incubation at 37°C with constant movement for
445 12 min or when cysts were broken up into single cells, dissociation was stopped by mixing with Soybean Trypsin
446 Inhibitor solution (Sigma, T6522; stock at 10 mg/ml in distilled water) at 1 mg/ml and centrifugation for 2 min
447 at 120 g, RT. The pellet was resuspended in N2B27 medium, filtered through a 40 µm cell strainer (BS
448 Biosciences, 352340) and 300.000 cells per insert were plated onto Matrigel-coated Transwells (Corning, 3470;
449 coating: incubation for 1 h at room temperature or 15 min at 37°C with Growth Factor-Reduced Matrigel
450 (Corning, 356230) diluted 1:20 in DMEM/F12 (Gibco, 31330-038), using 105 µl per transwell). The lower chamber
451 was filled RPE medium (DMEM+GlutaMAX (Gibco, 31966-047), 20% Knockout Serum Replacement (Gibco,
452 10828010), 0.5x L-Glutamine (Life Technologies, 25030-024), 1x MEM NEAA (Gibco, 11140-035), 0.1 mM ß-
453 mercaptoethanol (Gibco, 11528926), 1x Penicillin-Streptomycin (Gibco, 15140-122), 10 ng/ml Activin A (R&D
454 Systems, 338-AC; stock at 10 µg/ml in 4 mM HCl)) and 24 h after plating as well as every 2-3 days thereafter,
455 medium in both upper and lower chamber was exchanged to fresh RPE medium. At this stage, cells were
456 considered passage (P) 0.

457 *Passaging*

458 At 21 days after plating to P0 (protocol D26), cells were passaged to P1 and another 21 days later
459 (protocol D47) to P2. For passaging, cells were washed and incubated with Trypsin in both upper and lower
460 chamber for 10 min at 37°C, released from the transwells by pipetting up and down ~12 times with a 100 µl tip
461 and collected in warm RPE medium with 1 mg/ml Soybean Trypsin Inhibitor. The pellet of 3 min centrifugation
462 at 800 rpm was resuspended in fresh RPE medium, filtered through a 40 µm cell strainer and plated onto fresh
463 Matrigel-coated transwells at 600.000 cells per insert for P1 and 300.000 cells per insert for P2. Medium in both
464 upper and lower chamber was changed every 2-3 days.

465 *Cell release for sequencing and transplantation*

466 For analysis and transplantation, P1 and P2 cells were retrieved from the inserts as for passaging. After
467 centrifugation, cells were resuspended in RPE medium, filtered, counted and placed on ice until further use. For
468 transplantation, cells were centrifuged again for 2 min at 200 g and resuspended at a concentration of 50,000
469 or 100,000 cells/µl in MACS buffer (PBS (Gibco, 10010-023), 2 mM EDTA, 0.5% w/v BSA) supplemented with 0.1
470 mg/ml DNaseI (Sigma, D5025-150KU).

471 ## Sequencing

472 *RNA preparation*

473 To collect cells for sequencing, cells were detached from the transwell and processed as described
474 above. 150,000 cells were then lysed in 200 µl RLT buffer (Qiagen, 79216), flash frozen and stored at -70°C until
475 processing. RNA was isolated using the Qiagen RNeasy Mini RNA isolation kit (Qiagen, 74104) as instructed.
476 Briefly, lysed samples were thawed on ice, the RNA precipitated with an equal volume of 70% ethanol and the
477 sample transferred to an RNeasy spin column. After drying by centrifugation, a wash with Buffer RW1 and an
478 on-column DNase digestion, the column was washed again with Buffer RW1, then Buffer RPE and finally RNA
479 was eluted in water. All centrifugation steps were carried out for 30 s at 12,000 g. RNA integrity and
480 concentration was measured using an Agilent 2100 Bioanalyzer System with the RNA 6000 Pico Kit (Agilent
481 Technologies, 5067-1513).

482 *Library preparation and Sequencing*

483 mRNA was isolated from 100 or 500 ng total RNA by poly-dT enrichment using the NEBNext Poly(A)
484 mRNA Magnetic Isolation Module (NEB) according to the manufacturer's instructions. Samples were then
485 directly subjected to the workflow for strand-specific RNA-Seq library preparation (Ultra II Directional RNA
486 Library Prep, NEB). For ligation, the NEB Next Adapter for Illumina of the NEBNext Multiplex Oligos for Illumina
487 Kit was used at a final concentration of 0.004 or 0.016 µM. After ligation, adapters were depleted by XP bead
488 purification (Beckman Coulter), adding bead solution at a ratio of 0.9:1 to the samples (0.9X). Unique dual
489 indexing was done during the following PCR enrichment (12 or 14 cycles) using amplification primers carrying
490 the same sequence for i7 and i5 index (i5: AAT GAT ACG GCG ACC ACC GAG ATC TAC AC NNNNNNNN ACA TCT
491 TTC CCT ACA CGA CGC TCT TCC GAT CT, i7: CAA GCA GAA GAC GGC ATA CGA GAT NNNNNNNN GTG ACT GGA
492 GTT CAG ACG TGT GCT CTT CCG ATC T). After two more XP bead purifications (0.9X), libraries were quantified
493 using the Fragment Analyzer (Agilent). Libraries were sequenced on an Illumina NovaSeq 6000 in 100 bp paired-
494 end mode to an average depth of 40 million fragments per library.

495 *Bioinformatics – adapted version*

496 FastQC (http://www.bioinformatics.babraham.ac.uk/) was used to perform a basic quality control of
497 the resulting sequencing data. Fragments were aligned to the human reference genome GRCm38 with support
498 of the Ensembl 98 splice sites using the aligner gsnap (v2021-12-17) (Wu & Nacu, 2010). Counts per gene and
499 sample were obtained based on the overlap of the uniquely mapped fragments with the same Ensembl
500 annotation using featureCounts (v2.0.1) (Liao *et al*, 2014). Raw counts of technical replicates were averaged and
501 low count genes filtered out. For PCA analysis, data was transformed using the variance stabilizing

502 transformation function of the DESeq2 package (v1.42.1) (Love *et al*, 2014) and batch-corrected using the limma
503 package (v3.58.1) (Ritchie *et al*, 2015). To identify differentially expressed genes (DEGs) between cell passage
504 stages, counts were fitted to the negative binomial distribution and genes were tested between conditions using
505 the Wald test of DESeq2 package including the batch as a covariate. Genes with a maximum of 5% false discovery
506 rate (padj ≤ 0.05) were considered as significantly differentially expressed.

507 For GO term analysis DEGs were ordered by decreasing log2 fold change and used as input for an
508 ordered query with gprofiler2 (package v0.2.3, version e111_eg58_p18_f463989d) with g:SCS multiple testing
509 correction method applying significance threshold of 0.05 (Kolberg *et al*, 2020, 2023; Raudvere *et al*, 2019). To
510 limit the number of resulting terms, only DEGs upregulated in P1 cells with a log2 fold change > 3 were used,
511 while no log2 fold change threshold was applied for DEGs upregulated in P2 cells. Using the gprofiler2 web
512 application, resulting GO terms were grouped according to their connectivity in the GO context tab, with each
513 context group bearing the name of the contributing term with the lowest p-value. Context groups were again
514 thematically aggregated and z-scores of the regularized log-transformed data of the DEGs contributing most to
515 each aggregate were plotted as heatmaps.

516 Cell Surface Marker Screening

517 P1 RPE cells derived from CRTD1 iPSC were screened for expression of 371 antibodies directed against
518 cell surface markers using the flow cytometry-based MACS® Marker Screen, anti-human, version 01 (Miltenyi
519 Biotec, 130-110-055) according to the manufacturer's instructions. Undifferentiated CRTD1 and MIL001-A pre-
520 labelled with the CellTrace Violet Cell Proliferation Kit (Life Technologies, C34557) were pooled together with P1
521 RPE and used as internal control and reference. Data acquisition was done on MACSQuant Analyzer 10 (Miltenyi
522 Biotec, 130-096-343). MACS Quantify Software (Miltenyi Biotec) was used for analysis. Debris was excluded
523 based on scatter properties. Dead cells were excluded based on propidium iodide staining. RPE cells were gated
524 based on negative CellTrace Violet signal. Sidescatter (SSC) signal, as proxy for pigmentation, was used to gate
525 target (pigmented) and non-target cells (unpigmented). Full gating strategy and raw data is available as
526 supplementary data (Doc. S4). Combinations of candidate markers for pigmented and unpigmented cells were
527 validated on independent P1 RPE specimen.

528 For cell surface marker screening at Miltenyi Biotec Co., iPSC-derived P1 RPE differentiated by the Ader
529 lab using the standard protocol as described above were sent as frozen vials and used for screening directly after
530 thawing in cultivation medium (DMEM/F12, GlutaMAX (Gibco, 10565018), 20% Knockout Serum Replacement
531 (Gibco, 10828028), 0.8 mM L-Glutamine (Fagron, 700846), 1x MEM NEAA (Lonza, 13-114E), 0.1 mM ß-
532 mercaptoethanol (Sigma, M7522), 1x Penicillin/Streptomycin (Lonza, 17-602E), 10 ng/ml Activin A (Miltenyi,
533 130-115-010)) freshly supplemented with 10 µM StemMACS Y-27632 (Miltenyi, 130-106-538) and 1.5% Enzyme
534 Mix 2 from the Neural Tissue Dissociation Kit – Postnatal Neurons (Miltenyi, 130-094-802). Cell count was
535 determined using the flow cytometer MACSQuant Analyzer 10 (Miltenyi, 130-096-343) and viability assessed
536 with Propidium iodide (Miltenyi, 130-093-233).

537 ## Cell Surface Marker Sorting

538 ### *Live cell staining*

539 1x10^6 cells were stained in 100 µl cultivation medium or RPE medium (see RPE differentiation protocol)
540 supplemented with 10 µM StemMACS Y-27632 and 1.5% Enzyme Mix 2. P1 cells were stained with CD54-APC
541 (Miltenyi, 130-121-342) and PSA-NCAM-PE (Miltenyi, 130-117-394) according to data sheet. For washing steps,
542 supplemented medium was used and cells were centrifuged 5 min at 200 g.

543 ### *Sorting using the Tyto platform*

544 Cells in supplemented medium were sorted at a maximum concentration of 1x10^6 cells/ml in the
545 MACSQuant Tyto cell sorter (Miltenyi, 130-103-931) using a Tyto HS cartridge (Miltenyi, 130-121-549). Before
546 sorting, the cartridge was primed using the priming fixture according to protocol and 200-400 µl supplemented
547 medium. Cells were filtered over a 20 µm pre-separation filter (Miltenyi, 130-101-812) into the Tyto cartridge
548 via a 10 ml syringe with luer lock tip (Braun, 4617100V-02). For later analysis, an unsorted sample was taken
549 from the input chamber of the cartridge using a 200 µl gel loading tip (VWR, 732-2671). The sort was performed
550 in the MACSQuant Tyto cell sorter using software 1.0.0.

551 After the sort, fractions were retrieved from sort (target cell-enriched fraction, ENR) and non-sort
552 (target cell-reduced fraction, RED) chambers using 200 µl gel loading tips and both collection chambers were
553 washed with supplemented medium. Samples from all fractions were analyzed with a MACSQuant Analyzer 10
554 (Miltenyi, 130-096-343). Viability was determined using propidium iodide (Miltenyi, 130-093-233) or DAPI.
555 MACS Quantify Software (Miltenyi) was used to analyze the sort performance.

556 ### *Sorting using the Aria III platform*

557 For sorting of cells with the BD FACSAria III (BD Biosciences), stained cells were resuspended in
558 MACS/DNaseI buffer (PBS (Gibco, 10010-023), 2 mM EDTA, 0.5% w/v BSA, 0.1 mg/ml DNaseI (Sigma, D5025-
559 150KU)) and an UNS fraction was set aside. The gating strategy included gating out of debris (FCS-A v. SSC-A),
560 doublets (FSC-A v. FSC-H, SSC-H v. SSC-W) and dead cells based on DAPI uptake. Sorting was performed at 4°C,
561 using a 100 µm nozzle.

562 ### *Cell preparation for transplantation*

563 For transplantation, UNS, ENR and RED fractions obtained from both Tyto or Aria III were centrifuged
564 for 2 min at 200 g and resuspended at a concentration of 50,000 cells/µl in MACS/DNaseI buffer.

565 ### *Plating of sorted cells*

566 24-well transwell plates (Merck, CLS3470) were coated with Matrigel (Corning, 354234), diluted 1:20 in
567 D-MEM/F-12 (Gibco, 11320-074) on the previous day, using 120 µl of coating solution per well. Coating solution
568 was removed before plating 300.000 cells per 24-Transwell. Duplicates from unsorted cells (UNS), positive
569 sorted (ENR) and negative sorted (RED) fractions were plated. Cells were plated in upper part of the transwell in
570 200 µl cultivation medium containing 10 µM StemMACS Y-27632. The lower part was filled with 600 µl
571 cultivation medium. Medium was changed every 3-4 days (cultivation medium without Y-Compound).

572 ## Transplantation

573 Subretinal transplantation was performed as described in detail in (Tessmer *et al*, 2023). Briefly, mice
574 were anesthetized by intraperitoneal injection of 30 µg/kg bodyweight (bw) Ketamine (medistar, 04-03-
575 9264/23) and 1 µg/kg bw Medetomidine hydrocholoride (Orion Pharma, Domitor®) in sterile isotonic solution
576 (Fresenius Kabi, B306175/03), followed by application of dilating eye drops containing 2.5% phenylephrine and
577 0.5% tropicamide (University Clinic Pharmacy Dresden). After 1-2 min, eye drops were replaced with clear
578 moisturizing eye gel (Bausch+Lomb, Vidisic) and a coverslip placed on top for visibility through the operating
579 microscope. The mouse head was fixed with a stereotactic head holder (World Precision Instruments, 505242).
580 Using a sterile 30G needle, a small incision was made below the ora serrata opposite to the transplantation
581 target region. 1 µl cell suspension and 0.2 µl air were loaded into a 5 µl Hamilton syringe (Hamilton, 065-7634-
582 01) with a blunt 34-gauge needle (Hamilton, special request; 12 mm length). The Hamilton syringe was mounted
583 onto a micromanipulator (H. Saur Laborbedarf, M1) and the needle steered through the pre-made incision, until
584 it reached the retina at the target region. There, the air was used to generate a pre-bleb, followed by the
585 subretinal release of the cell suspension and slow needle retraction for self-sealing of the injection site.
586 Transplantation success and possible bleeding was noted and only eyes with an estimated ≥80% of cell
587 suspension successfully placed subretinally were considered in the experiments.

588 Immediately after transplantation, 80 µg filtered triamcinolone acetonide (University Clinic Pharmacy
589 Dresden; 80 µg/µl in NaCl, preservative-free, filtered through 35 µm mesh) were injected vitreally through the
590 same incision using a handheld 10 µl Hamilton syringe (Hamilton, 065-7635-01). Then, animals were released
591 from the head holder, intraperitoneally injected with 10 mg/kg bw atipamezole hydrochloride (Orion Pharma,
592 Antisedan®), placed in a warmed cage and monitored until fully awake.

593

594 ## Immunohistochemistry

595 ### *Sample collection and preparation*

596 Cultured cells were briefly washed in PBS and fixed by 10 min incubation in 4% paraformaldehyde (PFA)
597 in PBS at room temperature (RT). Cell-carrying membranes were cut out and either stained directly for the en
598 face view or embedded in NEG50 (Richard-Allan Scientific, 6502), frozen and cryosectioned with the Epredia™
599 CryoStar™ NX70 (Leika Mikrosysteme, Wetzlar, Germany) in 12 µm sections. Sections were air-dried at 37°C for
600 20 min and stained directly.

601 Experimental animals were anesthetized with isoflurane and decapitated. Eyes were enucleated
602 immediately and placed in 4% PFA in PBS for fixation over the course of 1 hour at 4°C. Samples for cryosectioning
603 were then dissected, removing lens and cornea, and cryoprotected overnight at 4°C in 30% w/v sucrose solution
604 in PBS. After embedding in NEG50 and freezing, eyes were serially sectioned at 12 µm thickness with the
605 CryoStar™. Sections were air-dried at 37°C for 20 min, stored at -70°C and allowed to come to RT before staining.

606 For flatmounts, fixed eyes were dissected removing lense, cornea and ocular muscle tissue. Then, the
607 retina was detached by cutting right below the ora serrata and incisions were made, cutting the eyball into petals
608 to allow later flattening. Flatmounts were stained immediately after collection.

609 *Staining*

610 All immunohistochemistry samples were blocked in blocking solution (0.3% Triton X-100, 1% bovine
611 serum albumin, 5% normal goat serum) for 1 h at RT and incubated overnight at 4°C with primary antibodies
612 idluted in blocking solution. After washing with PBS, samples were incubated for 1-2h in PBS containing
613 secondary antibodies and 0.2 µg/ml 4',6-diamidino-2-phenylindole (DAPI). Samples were washed again with PBS
614 and then distilled water before mounting using AquaPolymount (Polysciences, 18606).

615 ## Imaging and Image analysis

616 Stained cryosections were imaged with an Axio Imager.Z1 microscope with the ApoTome.2 enabled
617 (Zeiss). Unless noted otherwise, single images shown are maximum intensity projections of z-stacks with 5-6 µm
618 thickness. Flatmounts were imaged using the tiling setup of the Observer.Z1 microscope with the ApoTome.2
619 enabled (Zeiss), with z-stack depths of ca. 35 µm to ensure proper graft visualization despite a wavy surface.

620 For graft size and monolayer coverage quantification, every fourth serial section containing human
621 graft cells stained with an antibody against human nuclei was imaged with an AxioScan.Z1 (Zeiss). The graft
622 length per section was measured using the active curve tool, differentiating between monolayer and cluster
623 graft regions. Monolayer percentage was calculated dividing the sum of monolayer length measurements by the
624 sum of total graft measurements. The retinal coverage was calculated by diving total graft length by total retina
625 length. For total retina length, a standardized value was used, averaged from three eyes in which retina length
626 was measured after imaging serial sections of the entire eye.

627 Flatmount analysis with REShAPE was carried out using the code published on github (see key resources
628 table), adapted to run on the local server infrastructure.

629 All images were processed for visualization using Fiji (Schindelin *et al*, 2012).

630 ## Electron Microscopy (EM)

631 Eyes to be analyzed through TEM were collected from the animals as described for
632 immunohistochemistry. After fixation in 4% PFA in 100 mM phosphate buffer for 20-24 h, cornea, iris, lens and
633 muscle tissue were cut away and the globe was halved along the vertical axis (temporally located scar tissue
634 from the incision below the ora serrata during transplantation allowed for proper orientation). The nasal portion
635 containing the area of interest was further processed for EM as described in (Völkner *et al*, 2019; Gasparini *et*
636 *al*, 2022).

637 *Transmission Electron Microscopy (TEM)*

638 For TEM, the samples were further dissected to small pieces (0.5-1 mm) and postfixed at least overnight
639 in Modified Karnovsky's Fixative (2% glutaraldehyde, 2% paraformaldehyde in 100 mM phosphate buffer) at 4°C.
640 Samples were further postfixed and contrasted following the OTO-procedure by incubating them in a 2% OsO_4
641 solution (2% OsO4, 1.5% potassium ferrocyanide, 2 mM CaCl2 in water), then in 1% aqueous thiocarbohydrazide,
642 followed by another osmium step in 2% aqueous OsO_4 with washes in water between all incubation steps.
643 Finally, samples were *en-bloc* contrasted with 1% uranyl acetate in water, and washed several times in water.
644 Contrasted samples were then dehydrated in a graded ethanol series from 30% to 100% on a molecular sieve
645 (30%, 50%, 20 min each, 70%, 90%, 95%, 3x 100%, 30 min each), before embedding in EMBed 812 through

646 stepwise infiltration (25%, 50%, 75% resin 1h each, pure resin overnight, pure resin 5 h) and curing at 65°C
647 overnight. Semithin sections were made and stained with toluidine blue/borax to find the graft region. For TEM,
648 70 nm ultrathin sections were cut with a Leica UC6 ultramicrotome using a diamond knife (Diatome), collected
649 on formvar-coated slot grids and contrasted once more with lead citrate(Venable & Coggeshall, 1965) and uranyl
650 acetate. Samples were then imaged with a Jeol JEM1400 Plus transmission electron microscope (camera: Ruby,
651 Jeol) running at 80 kV acceleration voltage.

652 *Correlative light and electron microscopy (CLEM)*

653 CLEM samples were stored in 1% PFA in PBS, 4°C until selection and dissection of the ROIs under a
654 fluorescence stereo microscope (Leica MZ10F). Selected ROIs were subjected to progressive lowering of
655 temperature embedding in the methacrylate resin Lowicryl K4M (Carlemalm *et al*, 1982). Samples were
656 dehydrated in a graded ethanol series (30%, 50% ethanol/water 30 min each at 4°C, 70%, 90% at -20°C, 96% 1h
657 at -35°C, 2x 100% on molecular sieve at -35°C, 1h each. The last dehydration steps at -35°C and the following
658 infiltration steps in Lowicryl K4M (1:2 resin:ethanol, 1:1, and 2:1 for 1-2 h each, pure resin overnight, pure resin
659 5-6 h, all at -35°C) were conducted in a Leica AFS2 freeze substitution unit. Samples were placed and oriented
660 in flat embedding forms and cured by UV-irradiation at -35°C for 48 h. 70 nm ultrathin sections were cut using
661 a Leica UC6 ultramicrotome with a diamond knife, mounted onto formvar-coated mesh grids and
662 immunolabeled as described previously (Eberle *et al*, 2012; Fabig *et al*, 2012; Tranfield *et al*, 2024). Briefly,
663 sections were blocked with 1% BSA in PBS, sequentially incubated with the primary antibody (rabbit anti-GFP,
664 TP401 from Torrey Pines, 1:100) followed by protein A 10 nm gold (Utrecht CMC, 1:50), a fluorophore-
665 conjugated secondary antibody (goat-anti-rabbit Alexa488, 1:100) for immunofluorescence, and DAPI to
666 counterstain the nuclei. In between incubations, sections were washed with PBS, and labeled grids were then
667 mounted in glycerol-water (1:1) before fluorescent imaging with a Keyence Biozero 8000 fluorescence
668 microscope. Grids chosen for TEM were demounted, washed thoroughly in water, contrasted with uranyl
669 acetate, dried and imaged as described above for TEM samples.

670 ### Statistical Analysis

671 All values are represented as mean ± SEM (standard error of the mean) unless otherwise stated, with n = number
672 of retinas examined, where appropriate. Statistical significance was assessed using RStudio and denoted as $p <$
673 0.05 = *; $p < 0.01$ = **; $p < 0.001$ = ***. Samples were tested for outliers using Grubbs or Dixon test, and outliers
674 were removed before further analysis. Sample distributions were tested for normality using the Shapiro-Wilk's
675 test, and for homoscedacity using Bartlett's and Levene's test. Appropriate statistical tests were then applied
676 including: unpaired t-test, and Kruskal-Wallis with pairwise Wilcoxon test. Figs. were generated in Affinity
677 Designer.

678 ## Data Availability Section

679 This study includes no data deposited in external resources.

Acknowledgements

The authors would like to thank the Stem Cell Engineering, Flow Cytometry, Animal facility, Light Microscopy and Genome Center at the CRTD/CMCB, Technische Universität Dresden for assistance in iPSC cell culture, cell sorting, mouse maintenance, microscopy and sequencing/bioinformatic analysis, respectively. Additional technical and laboratory assistance was provided by Jochen Hentschel and Patrick Schäfer and IT assistance by Alexandre Mestiashvili. This work was supported by the Bundesministerium für Bildung und Forschung (BMBF): ReSight - 01EK1613A to M.A., 01EK1613C to S.K.), and Foundation Fighting Blindness (FFB Award Number: TA-RM-0522-0824-TUD-TRAP to M.A.).

Author contributions

K.T. & S.J.G.: Conceptualization, Methodology, Validation, Formal Analysis, Investigation, Writing – Original Draft, Writing – Review and Editing, Visualization, Supervision, and Project Administration. K.S.: Conceptualization, Methodology, Validation, Formal Analysis, Investigation, Visualization, and Project Administration. T.A. & L.M.: Validation and Investigation. J.H.: Validation, Formal Analysis, Investigation, Visualization, Supervision, and Project Administration. L.R.L, A.L., N.C.: Investigation and Resources. M.C.: Formal Analysis and Investigation. S.A.: Methodology and Resources. S.F., A.D., A.F.: Resources. T.K., A.P., U.A.F.: Formal Analysis. A.K.: Formal Analysis, Investigation, Resources and Supervision. H.J.: Formal Analysis, Resources, Writing – Original Draft, Writing – Review & Editing, and Supervision. S.K.: Formal Analysis, Resources, Writing – Original Draft, Writing – Review & Editing, Supervision, Project Administration, and Funding Acquisition. M.A.: Conceptualization, Methodology, Writing – Original Draft, Writing – Review and Editing, Supervision, Project Administration, and Funding Acquisition.

Disclosure and competing interests statement

The authors declare that they have no conflict of interest.

References

Almedawar S, Vafia K, Schreiter S, Neumann K, Khattak S, Kurth T, Ader M, Karl MO, Tsang SH & Tanaka EM (2020) MERTK-Dependent Ensheathment of Photoreceptor Outer Segments by Human Pluripotent Stem Cell-Derived Retinal Pigment Epithelium. *Stem Cell Reports* 14: 374–389

Anderson BD, Lee TT, Bell BA, Wang T & Dunaief JL (2024) Optimizing the sodium iodate model: Effects of dose, gender, and age. *Experimental Eye Research* 239: 109772

Barral S, Ecklebe J, Tomiuk S, Tiveron M-C, Desoeuvre A, Eckardt D, Cremer H & Bosio A (2013) Efficient neuronal *in vitro* and *in vivo* differentiation after immunomagnetic purification of mESC derived neuronal precursors. *Stem Cell Research* 10: 133–146

Carido M, Zhu Y, Postel K, Benkner B, Cimalla P, Karl MO, Kurth T, Paquet-Durand F, Koch E, Münch TA, *et al* (2014) Characterization of a Mouse Model With Complete RPE Loss and Its Use for RPE Cell Transplantation. *Investigative Opthalmology & Visual Science* 55: 5431

References

714 Carlemalm E, Garavito RM & Villiger W (1982) Resin development for electron microscopy and an analysis of
715 embedding at low temperature*. *Journal of Microscopy* 126: 123–143

716 Chan F, Bradley A, Wensel TG & Wilson JH (2004) Knock-in human rhodopsin-GFP fusions as mouse models for
717 human disease and targets for gene therapy. *Proceedings of the National Academy of Sciences* 101:
718 9109–9114

719 Davis RJ, Alam NM, Zhao C, Müller C, Saini JS, Blenkinsop TA, Mazzoni F, Campbell M, Borden SM, Charniga CJ,
720 *et al* (2017) The Developmental Stage of Adult Human Stem Cell-Derived Retinal Pigment Epithelium
721 Cells Influences Transplant Efficacy for Vision Rescue. *Stem Cell Reports* 9: 42–49

722 Eberle D, Kurth T, Santos-Ferreira T, Wilson J, Corbeil D & Ader M (2012) Outer Segment Formation of
723 Transplanted Photoreceptor Precursor Cells. *PLoS ONE* 7: e46305

724 Fabig G, Kretschmar S, Weiche S, Eberle D, Ader M & Kurth T (2012) Chapter 5 - Labeling of Ultrathin Resin
725 Sections for Correlative Light and Electron Microscopy. In *Methods in Cell Biology*, Müller-Reichert T &
726 Verkade P (eds) pp 75–93. Academic Press

727 Farjood F, Manos JD, Wang Y, Williams AL, Zhao C, Borden S, Alam N, Prusky G, Temple S, Stern JH, *et al* (2023)
728 Identifying biomarkers of heterogeneity and transplantation efficacy in retinal pigment epithelial cells.
729 *Journal of Experimental Medicine* 220: e20230913

730 Fleckenstein M, Keenan TDL, Guymer RH, Chakravarthy U, Schmitz-Valckenberg S, Klaver CC, Wong WT & Chew
731 EY (2021) Age-related macular degeneration. *Nat Rev Dis Primers* 7: 1–25

732 Gasparini SJ, Tessmer K, Reh M, Wieneke S, Carido M, Völkner M, Borsch O, Swiersy A, Zuzic M, Goureau O, *et*
733 *al* (2022) Transplanted human cones incorporate into the retina and function in a murine cone
734 degeneration model. *J Clin Invest* 132

735 Gullapalli VK, Sugino IK, Van Patten Y, Shah S & Zarbin MA (2005) Impaired RPE survival on aged submacular
736 human Bruch's membrane. *Experimental Eye Research* 80: 235–248

737 Gupta S, Lytvynchuk L, Ardan T, Studenovska H, Sharma R, Faura G, Eide L, Shanker Verma R, Znaor L, Erceg S, *et*
738 *al* (2023) Progress in Stem Cells-Based Replacement Therapy for Retinal Pigment Epithelium: In Vitro
739 Differentiation to In Vivo Delivery. *Stem Cells Translational Medicine* 12: 536–552

740 Kim D-S, Lee DR, Kim H-S, Yoo J-E, Jung SJ, Lim BY, Jang J, Kang H-C, You S, Hwang D-Y, *et al* (2012) Highly Pure
741 and Expandable PSA-NCAM-Positive Neural Precursors from Human ESC and iPSC-Derived Neural
742 Rosettes. *PLOS ONE* 7: e39715

743 Klymenko V, González Martínez OG & Zarbin M (2024) Recent Progress in Retinal Pigment Epithelium Cell-Based
744 Therapy for Retinal Disease. *Stem Cells Translational Medicine*: szae004

745 Kolberg L, Raudvere U, Kuzmin I, Adler P, Vilo J & Peterson H (2023) g:Profiler—interoperable web service for
746 functional enrichment analysis and gene identifier mapping (2023 update). *Nucleic Acids Research* 51:
747 W207–W212

748 Kolberg L, Raudvere U, Kuzmin I, Vilo J & Peterson H (2020) gprofiler2 -- an R package for gene list functional
749 enrichment analysis and namespace conversion toolset g:Profiler.
750 doi:10.12688/f1000research.24956.2 [PREPRINT]

751 Lawrence JM, Sauvé Y, Keegan DJ, Coffey PJ, Hetherington L, Girman S, Whiteley SJO, Kwan ASL, Pheby T & Lund
752 RD (2000) Schwann Cell Grafting into the Retina of the Dystrophic RCS Rat Limits Functional
753 Deterioration. *Investigative Ophthalmology & Visual Science* 41: 518–528

754 Liao Y, Smyth GK & Shi W (2014) featureCounts: an efficient general purpose program for assigning sequence
755 reads to genomic features. *Bioinformatics* 30: 923–930

Love MI, Huber W & Anders S (2014) Moderated estimation of fold change and dispersion for RNA-seq data with DESeq2. *Genome Biology* 15: 550

Nakai-Futatsugi Y, Jin J, Ogawa T, Sakai N, Maeda A, Hironaka K, Fukuda M, Danno H, Tanaka Y, Hori S, *et al* (2024) Pigmentation level of human iPSC-derived RPE does not indicate a specific gene expression profile. *eLife* 12: RP92510

Nguyen L, Rigo J-M, Malgrange B, Moonen G & Belachew S (2003) Untangling the Functional Potential of PSA-NCAM-Expressing Cells in CNS Development and Brain Repair Strategies. *Current Medicinal Chemistry* 10: 2185–2196

Ortolan D, Sharma R, Volkov A, Maminishkis A, Hotaling NA, Huryn LA, Cukras C, Di Marco S, Bisti S & Bharti K (2022) Single-cell–resolution map of human retinal pigment epithelium helps discover subpopulations with differential disease sensitivity. *Proceedings of the National Academy of Sciences* 119: e2117553119

Petrus-Reurer S, Lederer AR, Baqué-Vidal L, Douagi I, Pannagel B, Khven I, Aronsson M, Bartuma H, Wagner M, Wrona A, *et al* (2022) Molecular profiling of stem cell-derived retinal pigment epithelial cell differentiation established for clinical translation. *Stem Cell Reports* 17: 1458–1475

Plaza Reyes A, Petrus-Reurer S, Padrell Sánchez S, Kumar P, Douagi I, Bartuma H, Aronsson M, Westman S, Lardner E, André H, *et al* (2020) Identification of cell surface markers and establishment of monolayer differentiation to retinal pigment epithelial cells. *Nature Communications* 11: 1–15

Raudvere U, Kolberg L, Kuzmin I, Arak T, Adler P, Peterson H & Vilo J (2019) g:Profiler: a web server for functional enrichment analysis and conversions of gene lists (2019 update). *Nucleic Acids Research* 47: W191–W198

Ritchie ME, Phipson B, Wu D, Hu Y, Law CW, Shi W & Smyth GK (2015) limma powers differential expression analyses for RNA-sequencing and microarray studies. *Nucleic Acids Research* 43: e47

Schindelin J, Arganda-Carreras I, Frise E, Kaynig V, Longair M, Pietzsch T, Preibisch S, Rueden C, Saalfeld S, Schmid B, *et al* (2012) Fiji: an open-source platform for biological-image analysis. *Nat Methods* 9: 676–682

Schreiter S, Vafia K, Barsacchi R, Tsang SH, Bickle M, Ader M, Karl MO, Tanaka EM & Almedawar S (2020) A Human Retinal Pigment Epithelium-Based Screening Platform Reveals Inducers of Photoreceptor Outer Segments Phagocytosis. *Stem Cell Reports* 15: 1347–1361

Sharma R, Bose D, Montford J, Ortolan D & Bharti K (2022) Triphasic developmentally guided protocol to generate retinal pigment epithelium from induced pluripotent stem cells. *STAR Protocols* 3: 101582

Sharma R, Khristov V, Rising A, Jha BS, Dejene R, Hotaling N, Li Y, Stoddard J, Stankewicz C, Wan Q, *et al* (2019) Clinical-grade stem cell–derived retinal pigment epithelium patch rescues retinal degeneration in rodents and pigs. *Science Translational Medicine* 11: eaat5580

Singh MS, Charbel Issa P, Butler R, Martin C, Lipinski DM, Sekaran S, Barnard AR & MacLaren RE (2013) Reversal of end-stage retinal degeneration and restoration of visual function by photoreceptor transplantation. *Proceedings of the National Academy of Sciences* 110: 1101–1106

Strauss O (2005) The Retinal Pigment Epithelium in Visual Function. *Physiological Reviews* 85: 845–881

Tanaka E & Zhu Y (2015) Method for producing polarized retinal progenitor cells from pluripotent stem cells and their differentiation into retinal pigment epithelium cells.

Tessmer K, Borsch O, Ader M & Gasparini SJ (2023) Micromanipulator-Assisted Subretinal Transplantation of Human Photoreceptor Reporter Cell Suspensions into Mice. In *Brain Organoid Research*, Gopalakrishnan J (ed) pp 81–98. New York, NY: Springer US

References

798 Tranfield EM, Fabig G, Kurth T & Müller-Reichert T (2024) Chapter One - How to apply the broad toolbox of
799 correlative light and electron microscopy to address a specific biological question. In *Methods in Cell*
800 *Biology*, Müller-Reichert T & Verkade P (eds) pp 1–41. Academic Press

801 Venable JH & Coggeshall R (1965) A SIMPLIFIED LEAD CITRATE STAIN FOR USE IN ELECTRON MICROSCOPY.
802 *Journal of Cell Biology* 25: 407–408

803 Voigt AP, Whitmore SS, Flamme-Wiese MJ, Riker MJ, Wiley LA, Tucker BA, Stone EM, Mullins RF & Scheetz TE
804 (2019) Molecular characterization of foveal versus peripheral human retina by single-cell RNA
805 sequencing. *Experimental Eye Research* 184: 234–242

806 Völkner M, Kurth T & Karl MO (2019) The Mouse Retinal Organoid Trisection Recipe: Efficient Generation of 3D
807 Retinal Tissue from Mouse Embryonic Stem Cells. In *Retinal Degeneration: Methods and Protocols*,
808 Weber BHF & Langmann T (eds) pp 119–141. New York, NY: Springer

809 Wang S, Lu B, Girman S, Holmes T, Bischoff N & Lund RD (2008) Morphological and Functional Rescue in RCS
810 Rats after RPE Cell Line Transplantation at a Later Stage of Degeneration. *Investigative Ophthalmology*
811 *& Visual Science* 49: 416–421

812 Wu TD & Nacu S (2010) Fast and SNP-tolerant detection of complex variants and splicing in short reads.
813 *Bioinformatics* 26: 873–881

814 Xu Z, Liao X, Li N, Zhou H, Li H, Zhang Q, Hu K, Yang P & Hou S (2021) A Single-Cell Transcriptome Atlas of the
815 Human Retinal Pigment Epithelium. *Frontiers in Cell and Developmental Biology* 9

816 Zhu Y, Carido M, Meinhardt A, Kurth T, Karl MO, Ader M & Tanaka EM (2013) Three-Dimensional Neuroepithelial
817 Culture from Human Embryonic Stem Cells and Its Use for Quantitative Conversion to Retinal Pigment
818 Epithelium. *PLOS ONE* 8: e54552

819 Zhu Y, Schreiter S & Tanaka EM (2016) Accelerated Three-Dimensional Neuroepithelium Formation from Human
820 Embryonic Stem Cells and Its Use for Quantitative Differentiation to Human Retinal Pigment Epithelium.
821 In *Human Embryonic Stem Cell Protocols*, Turksen K (ed) pp 345–355. New York, NY: Springer

822 Zhu Y & Tanaka E (2016) Method for producing polarized retinal progenitor cells from pluripotent stem cells and
823 their differentiation into retinal pigment epithelium cells.

824

825

References

826

Figures and Figure legends

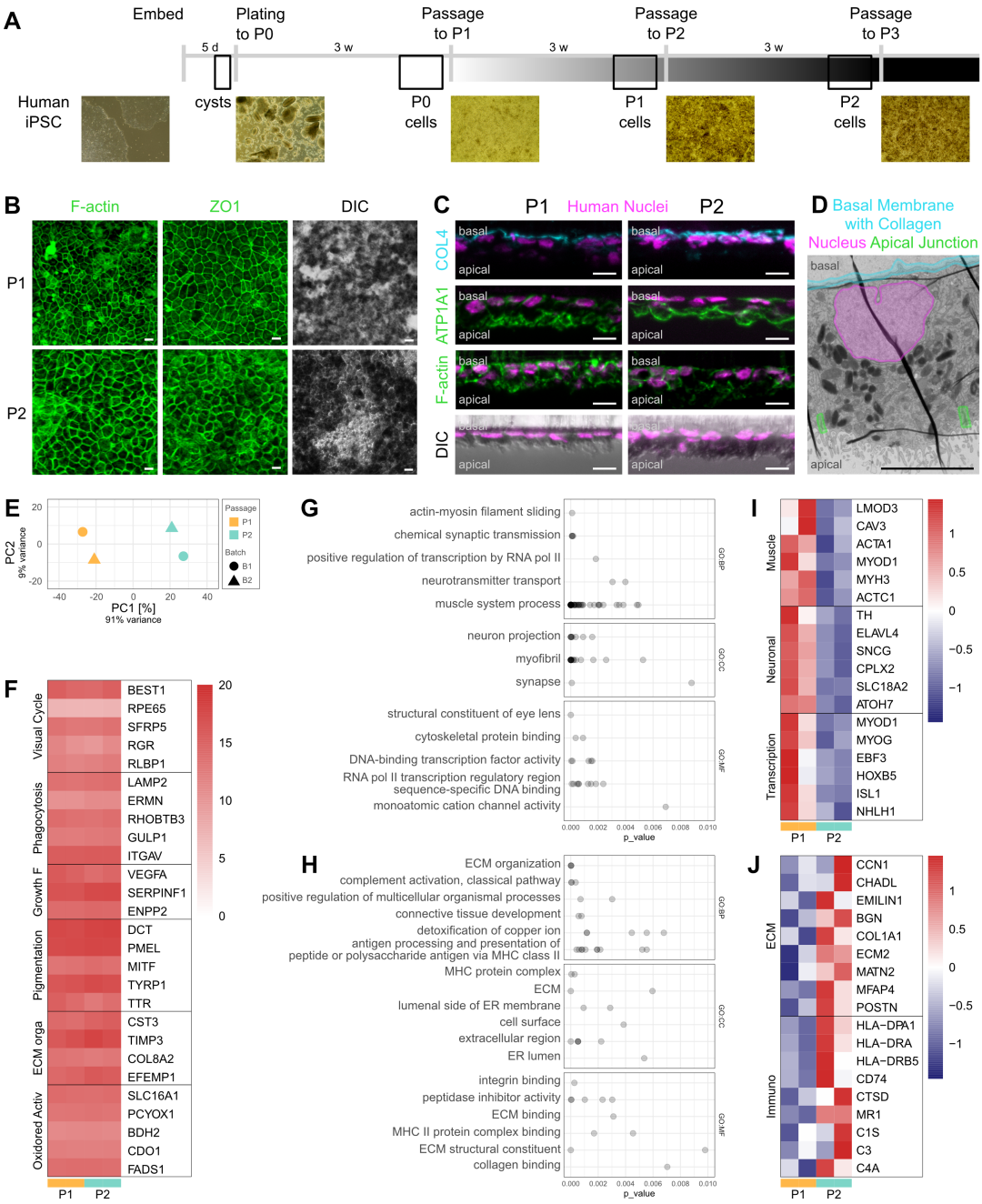

Figure 1: Characterization of P1 and P2 iPSC-derived RPE cells.

(A) Scheme for the differentiation of iPSCs into RPE cells and representative images from different stages. In brief, iPSCs formed cysts in Matrigel within 5 days (d), followed by plating in RPE induction medium for 3 weeks (w). Passaging to cell culture inlets and culture for 3 w yielded passage (P) 1 cells and, after an additional passage and another 3 w, P2 cells.

(B) P1 and P2 RPE cells form monolayers with cobblestone morphology visualized by immuno-fluorescence staining for F-actin or zonula occludens 1 (ZO1). P1 and P2 RPE cells are highly pigmented.

(C) Sections of P1 and P2 RPE monolayers show positive immunofluorescence staining for Human Nuclei, basally localized collagen IV (COL4), and apically localized ATPase (ATP1A1) and F-actin. Combined fluorescence staining (Human Nuclei) with DIC imaging reveals basal localization of RPE nuclei.

(D) Ultrastructure of differentiated P1 RPE cell showing features characteristic of polarized RPE monolayer features including a basal membrane with collagen (marked blue), a basally located nucleus (marked

842 magenta), apically located pigmented melanosomes, apical microvilli, and tight/adherens junction
843 (marked green).
844 (E) Principle component (PC) analysis after batch correction reveals close clustering of same passage number
845 cells across cell culture batches.
846 (F) Heatmap showing expression levels of RPE-related genes obtained by bulk RNAseq analysis from two batches
847 each of P1 and P2 RPE cells. Values shown are $\log_2$(normalized counts+1).
848 (G, H) Gene ontology (GO) term analysis of differentially expressed genes shows GO term groups
849 overrepresented in P1 (G) and P2 (H) cultures, respectively. Points represent single GO terms, grouped
850 together according to the GO context view of gprofiler2, under the grouping label of the GO term with
851 the lowest p-value. Overlapping points results in darker grey. Full GO term list and groupings are available
852 in Doc. S2. GO:BP, GO terms concerning biological processes; GO:CC, GO terms concerning cellular
853 components; GP:MF, GO terms concerning molecular functions.
854 (I, J) Heatmaps showing z-scores of the differentially expressed genes contributing most often to the GO terms
855 overrepresented in P1 (I) and P2 (J) cultures. Genes are aggregated according to their involvement in GO
856 terms related to muscular, neuronal and transcriptional (I) or extracellular matrix (ECM) and
857 immunologically relevant (J) terms.
858 Scale bars: 10 µm (B, C), 5 µm (D).

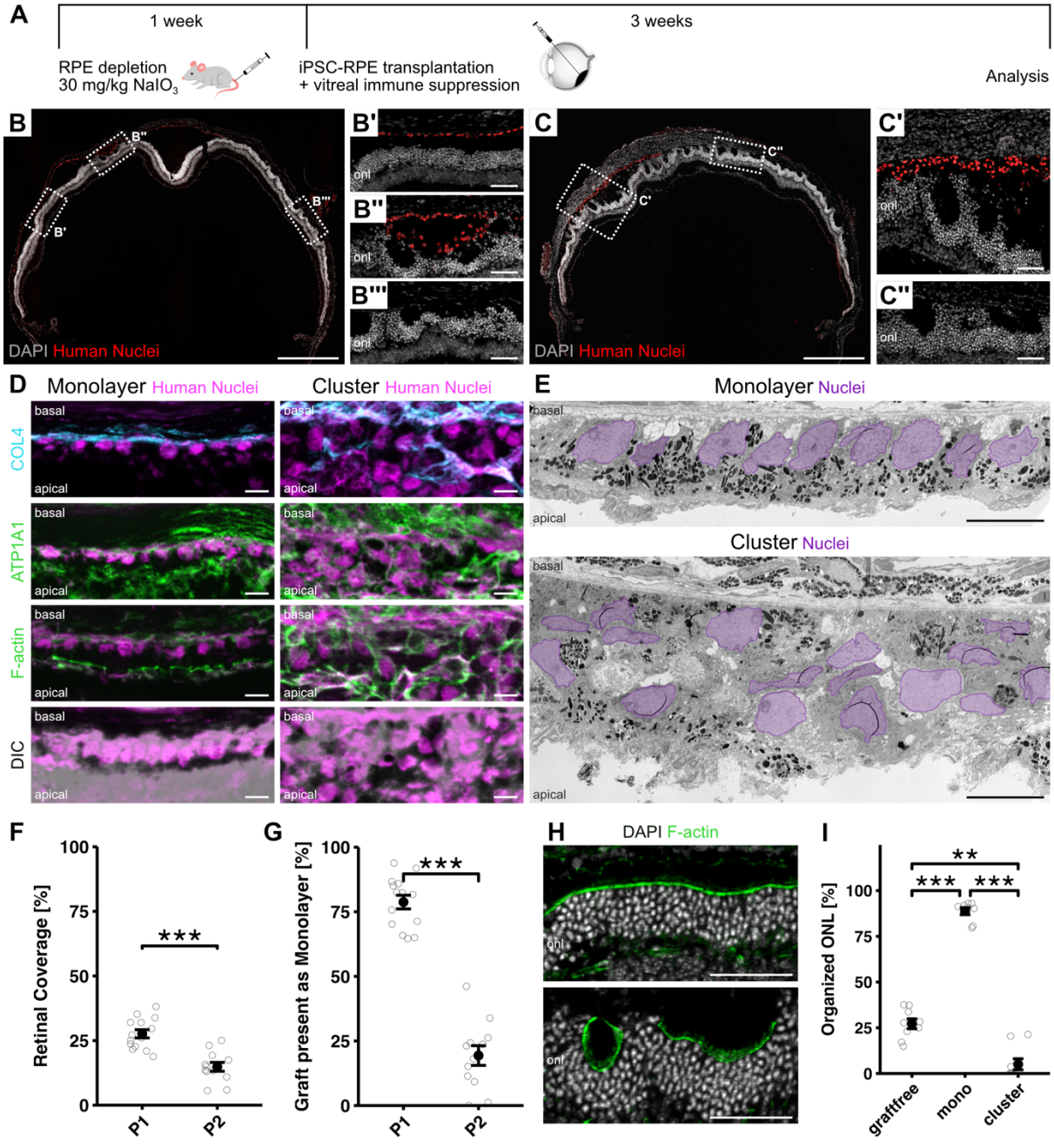

Figure 2: Single cell suspension transplantation of P1 but not P2 RPE yields large areas of polarized RPE monolayer

(A) Scheme of experimental design: Mice received a tail vein injection of 30 mg/kg bodyweight sodium iodate ($NaIO_3$) causing depletion of endogenous RPE. One week later, a suspension of P1 or P2 RPE cells was injected into the subretinal space and the immune suppressant triamcinolone acetonide was supplied vitreally. Experimental eyes were analysed 3 weeks post-transplantation.

(B) Representative section of a P1 RPE transplanted retina. Human-specific marker staining (Human Nuclei) revealed the survival of P1 RPE cells in large areas with many donor cells forming a monolayer-like structure between choroid and ONL (B, B') and some cells forming multilayered cell clusters (B, B''). While the ONL beneath donor cell-derived monolayers appears well organized (B, B'), the ONL beneath clusters or regions without RPE appears disorganized containing foldings and tubulations (B, B'', B'''). Cell nuclei counterstained with DAPI.

874 (C) Representative section of a P2 RPE transplanted retina. Human-specific marker staining (Human Nuclei)
875 revealed the survival of P2 RPE cells in large areas with most donor cells forming multi-layered cell
876 clusters and few monolayer-like structures (C, C'). The ONL beneath clusters or regions without RPE
877 appears similarly disorganized containing foldings and tubulations (C, C', C''). Cell nuclei counterstained
878 with DAPI.
879 (D) Immunofluorescence analysis of RPE-derived monolayers and clusters. RPE monolayers show positive
880 immunofluorescence staining for human nuclei, that have a 'pearls-on-a-string' appearance, basally
881 localized collagen IV (COL4), and apically localized ATPase (ATP1A1) and F-actin. Combined fluorescence
882 staining with DIC imaging reveals basal localization of RPE nuclei and strong pigmentation apically. In
883 clusters, human nuclei appear as multilayered, unorganized aggregates, that are positive for COL4,
884 ATPase and F-actin, but lack a clear basal-apical polarity.
885 (E) Ultrastructural analysis of human RPE-derived monolayers reveals apicobasal polarity including basally
886 localized nuclei, basal membrane/labyrinth and mitochondria, and apical melanosomes. Compare figure
887 S2 for details. Donor-derived clusters show a disorganized appearance without cell polarization.
888 (F) Retinal coverage of transplanted P1 and P2 RPE cells. Three weeks after transplantation, P1 donor RPE cells
889 covered almost double the host retinal surface as P2 RPE cells (P1: 27.6% ± 1.6%, n = 14; P2: 14.8% ±
890 1.7%, n = 12; two-sided t-test)
891 (G) P1 RPE cells exhibited a significantly larger proportion of the graft as monolayers than P2 RPE transplants
892 (P1: 78.8% ± 2.7%, n= 14; P2: 19.4% ± 3.8%, n = 12; two-sided t-test)
893 (H) Experimental retinas show areas with organized (top) and disorganized (bottom) ONL, visualized by the OLM
894 shown through staining for F-actin. In contrast to an organized ONL, a disorganized ONL shows foldings,
895 rosettes and tubulations (compare also DAPI staining in figures 2B' vs. 2B''- 2C'').
896 (I) Beneath donor RPE monolayers the majority of the ONL shows an organized structure, while the ONL beneath
897 graft-free or cluster areas is mainly disorganized (graft-free: 27.2%±2.7; n = 9; monolayer: 88.8%±1.9, n
898 = 8, cluster: 5.1%±3.0; n = 9; Kruskal-Wallis test with pairwise Wilcoxon test)
899 Scale bars: 500 µm (B, C), 50 µm (B'-B''', C', C'', H) and 10 µm (D, E). onl, outer nuclear layer. Data are represented
900 as mean ± SEM.

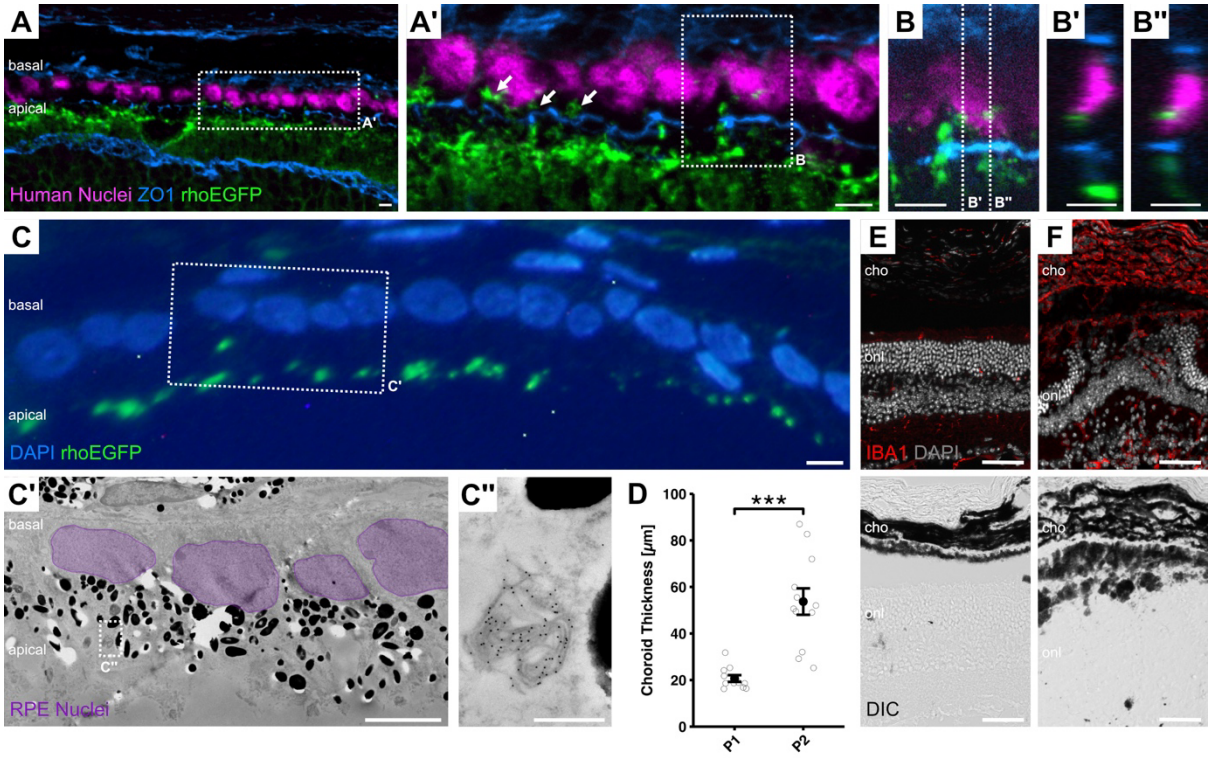

Figure 3: Donor RPE cells phagocytose photoreceptor outer segments and P2 cells induce strong immune reaction.

(A) Phagocytosed photoreceptor outer segments can be detected in human RPE monolayer cells (arrows) three weeks after transplantation into $NaIO_3$-treated rhoEGFP mice.

(B) Single plane of the z-stack area highlighted in A'. B shows the xy plane, B' and B'' show the zy planes at x positions marked in B.

(C) Correlative light- and electron-microscopy (CLEM) reveals host outer segment particles within transplanted RPE cells, visualized by immunofluorescent (C) and immunogold (C', C'') labelling of rhoEGFP protein three weeks after transplantation into the retina of $NaIO_3$ treated rhoEGFP mice.

(D) Retinas with P2 RPE donor cells show a significantly thicker choroid in comparison to P1 transplanted mice (C; P1: 20.7 µm ± 1.4, n = 11; P2: 53.7 µm ± 5.7, n = 12; two-sample Wilcoxon test), pointing to a stronger immune response triggered by P2 transplants.

(E, F) Retinas with P2 RPE donor cells (F) show increased numbers of ionized calcium-binding adapter molecule 1 $(IBA1)^+$ cells both within the retina and the choroid than retinas that received P1 RPE donor cells (E).

Scale bars: 50 µm (E, F), 5 µm (A-C') and 500 nm (C''). cho, choroid; onl, outer nuclear layer. Data are represented as mean ± SEM.

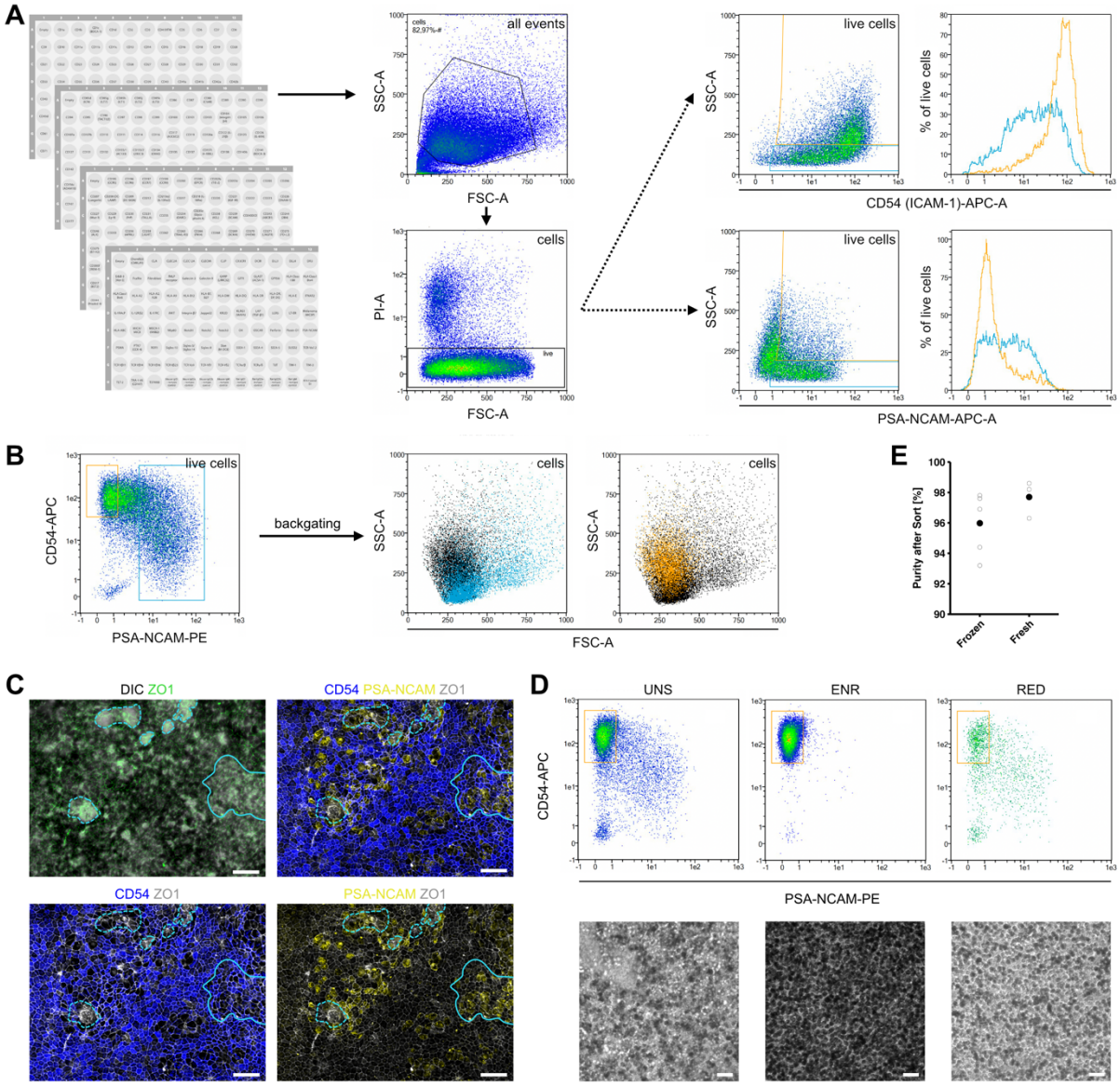

Figure 4: Identification and validation of cell surface sorting markers for iPSC-derived P1 RPE cells

(A) P1 RPE cells were screened for expression of 371 antibodies directed against cell surface markers using flow cytometry. Hits were identified based on correlation to side scatter (SSC) intensity as proxy for pigmentation, here shown for CD54 (ICAM-1) (positive correlation) and PSA-NCAM (negative correlation).

(B) Combinatorial staining for CD54 and PSA-NCAM reliably discriminates SSC-low non-target (unpigmented, backgated in blue) and SSC-high target cells (pigmented, backgated in orange).

(C) Immunofluorescent staining of RPE cells in culture shows cells expressing PSA-NCAM but little CD54 mostly in regions lacking pigmentation and proper cobblestone morphology (areas highlighted by dashed lines). Co-expression of CD54 and PSA-NCAM appears to occur primarily in regions of intermediate pigmentation levels and mixed cobblestone morphology (area highlighted by solid line).

(D) Flow scatter and corresponding transmitted light microscopy images for unsorted (UNS), $CD54^{+}$/PSA-$NCAM^{-}$-enriched (ENR) and $CD54^{+}$/PSA-$NCAM^{-}$-reduced (RED) cell fractions. Cells were sorted using the MACSQuant Tyto cell sorter to maximize target cell purity. Replated fractions reveal that pigmented cells can be efficiently enriched with the dual marker strategy.

(E) $CD54^{+}$/PSA-$NCAM^{-}$ sorting of frozen and freshly harvested cells consistently yielded a target fraction of high purity. Circles show single re-analysis measurements, solid points their average.

Scale bars: 100 µm (D), 50 µm (C).

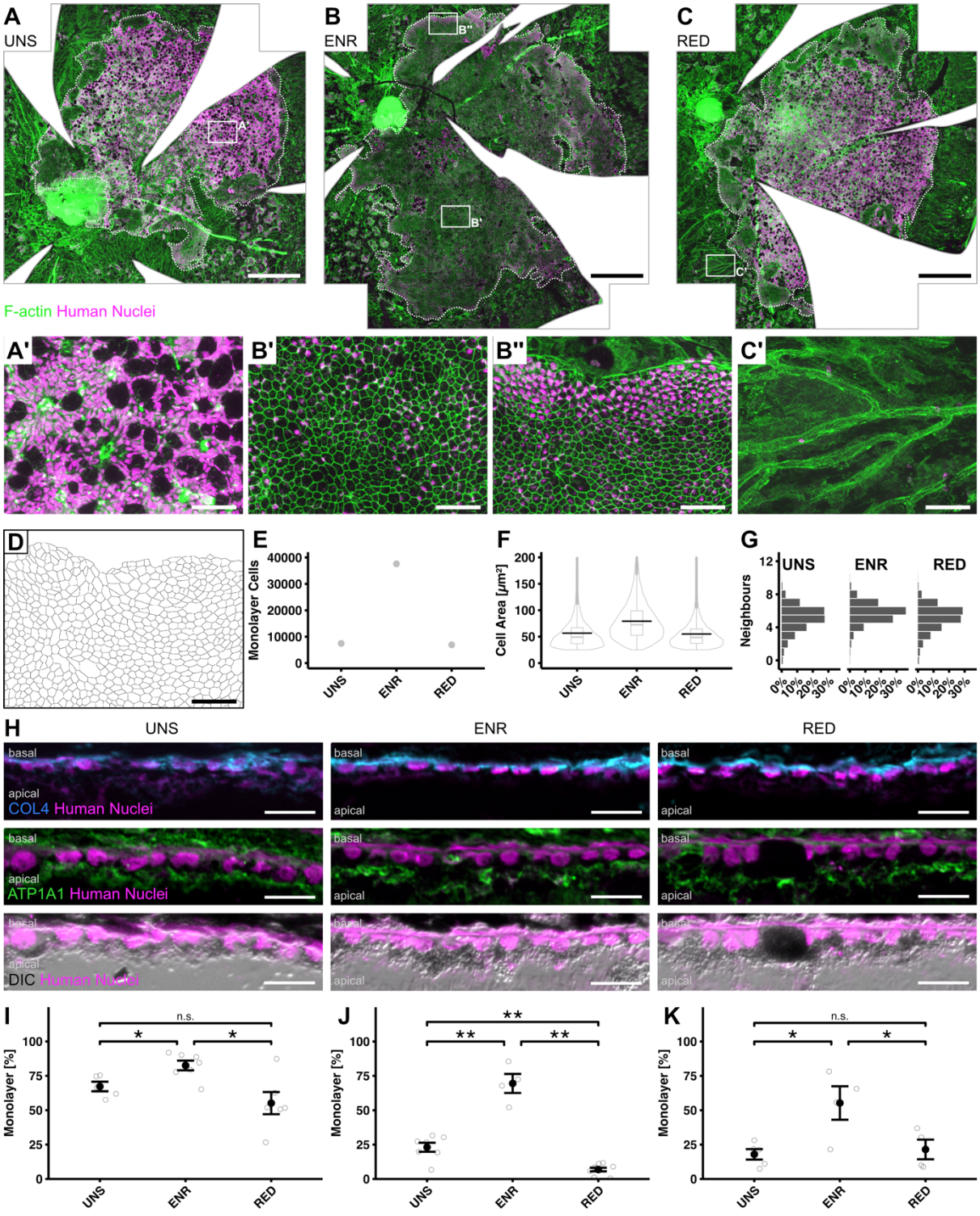

Figure 5: CD54⁺/PSA-NCAM⁻ RPE cells show increased monolayer formation after transplantation. (A – C) Flat-mounted eyecups that received P1 RPE single cell suspensions which were either unsorted (UNS; A), enriched (ENR, B), or reduced (RED, C) in CD54⁺/PSA-NCAM⁻ cells show large areas of donor cells identified by Human Nuclei staining (graft region outlined with dotted lines). While in UNS (A, A') and RED (C) samples the proportion of area with cell clusters (visible through intense Human Nuclei staining) is high, in ENR transplanted retinas the proportion of monolayer with typical cobblestone morphology as seen by staining for F-actin is high (B, B', B''). Human nuclei visibility in properly structured monolayers is concealed due to high pigmentation of donor cells (B''; for single z-planes see figures S4E and F), but better visible at monolayer edges (B'). Magnification of an RPE-depleted area without donor cells is shown in C'.

949 (D) Outlines of monolayer cells from B'' as detected with the REShAPE tool(Ortolan *et al*, 2022) show the
950 possibility to analyse the grafts in flatmount view.
951 (E-G) REShAPE analysis of the flatmounts A-C (corresponding REShAPE cell outline maps see figure S4G-I). (E)
952 reveals a highly increased number of monolayer cells in the ENR graft in comparison to UNS or RED (UNS:
953 7453, ENR: 37607, RED: 6921). ENR monolayer cells on average appear larger than UNS or RED monolayer
954 cells (F; mean areas: UNS 57 μm^2, ENR 79 μm^2, RED 55 μm^2, violin plots of all cells detected with overlaid
955 box-plots showing median and 25% quartiles, black lines showing the mean). In all three conditions
956 human monolayer cells have mostly 5 or 6 neighboring cells, with the ENR graft having the highest ratio
957 of cells with 5-7 neighbors (G; UNS: 67%, ENR: 82%, RED: 69%).
958 (H) Monolayers formed in all conditions show a polarized morphology with basal collagen IV (COL4) and apical
959 ATPase (ATP1A1) expression. Human nuclei are located basally, while pigmentation (dark in DIC images)
960 appears mainly apically. Large, highly pigmented, round structures are frequently detected in clusters
961 (see also A') and sometimes in monolayer areas, likely representing pigment-filled macrophages
962 (compare also figure S5A).
963 (I, J) Quantification of monolayer proportion after transplantation of RPE cells from two separate differentiation
964 rounds. While in both rounds the $CD54^+$/PSA-$NCAM^-$ ENR donor cell fractions robustly generated similarly
965 high proportions of monolayer (ENR - I : 82.5% ± 3.5%; n=7; ENR – J: 69.5% ± 6.9%; n=4), the amount of
966 monolayer generated by UNS (UNS - I: 67.3% ± 3.5%; n=5; UNS - J: 23.1% ± 3.3%, n=7) and RED cell
967 fractions (RED - I: 55.2% ± 8.1%; n=6; RED - J: 6.9% ± 1.3%, n=9; Kruskal-Wallis with pairwise Wilcoxon
968 test) strongly varied, correlating with different amounts of $CD54^+$/PSA-$NCAM^-$ cell purity within the
969 different fractions (see also figure S4A for purity data related to figure 5I and figure S4B for purity data
970 related to figure 5J).
971 (K) Quantification of monolayer proportion after transplantation of RPE cells from a third differentiation round,
972 sorted with conventional flow cytometry (UNS: 17.9% ± 3.8%, n = 5; ENR: 55.3% ± 12.2%, n = 4; RED:
973 21.5% ± 7.2%, n = 4; Kruskal-Wallis with pairwise Wilcoxon test).
974 Scale bars, 500 µm (A, B, C), 50 µm (A', B', B'', C', D) and 20 µm (H). Data are represented as mean ± SEM.

975
Supplemental document titles

976 Document S1. Figures S1-S5.

977 Document S2. Excel file containing raw counts, differentially expressed genes, GO terms and GO term
978 groups obtained from bulk sequencing of P1 versus P2 cells, related to Figure 1.

979 Document S3. PDF containing screening results of all cell surface antibodies tested with the MACS
980 Marker Screen, related to Figure 4

981

982
Supplemental figures and legends

983

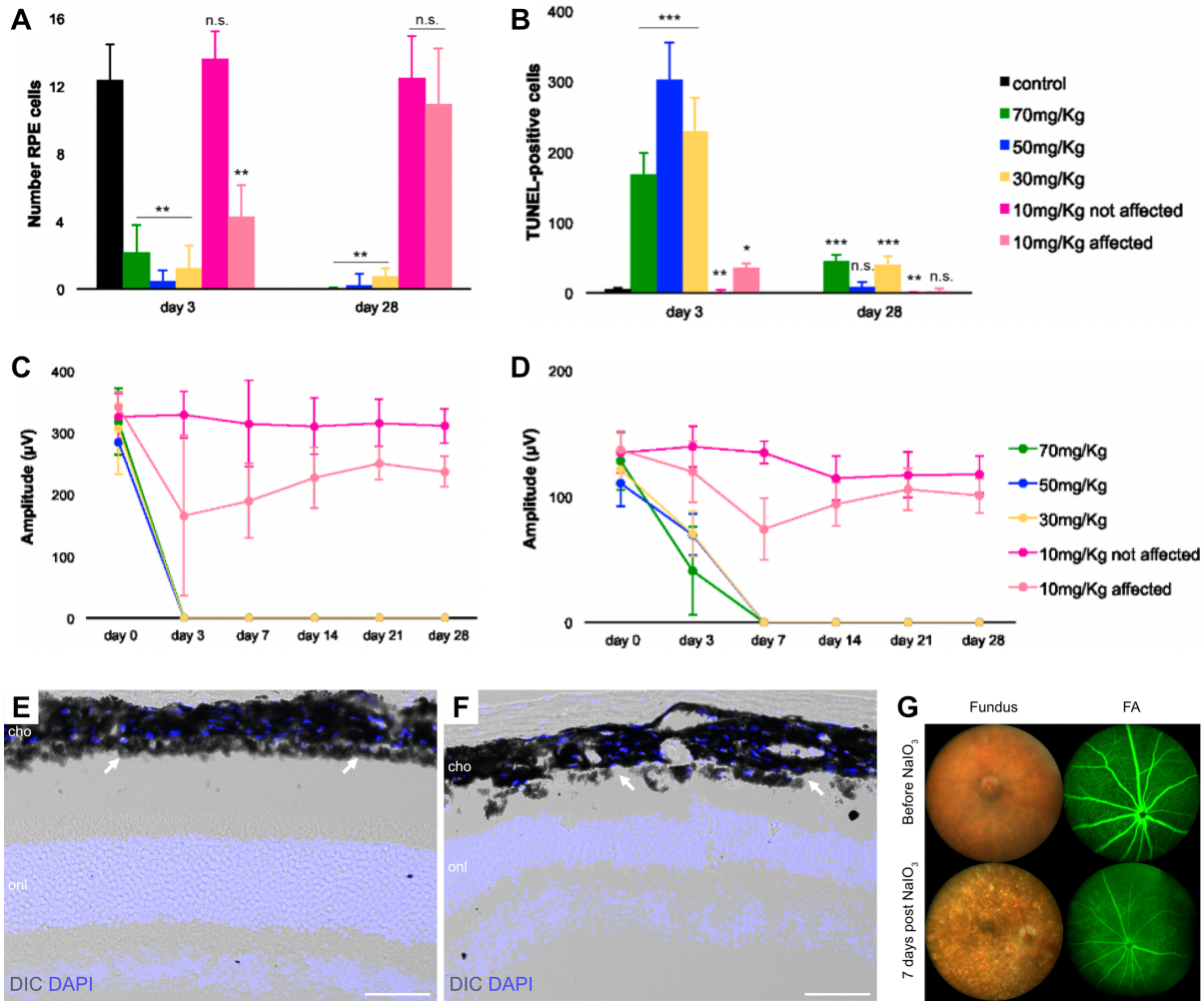

Figure S1: Injection of 30 mg/kg bodyweight $NaIO_3$ suffices to cause RPE degeneration and loss of visual function.
(A) While a low dosage (10 mg/kg bodyweight (bw) $NaIO_3$) had variable effects on RPE cell number, an injection of the intermediate dosage of 30 mg/kg bw $NaIO_3$ was sufficient to cause RPE degeneration to a similar degree as high dosages (50 and 70 mg/kg bw $NaIO_3$) at day 3 and day 28.
(B) In intermediate and high dosage groups, RPE cell death occurred quickly after $NaIO_3$ injection (day 3), and was strongly reduced at 4 weeks after injection (day 28).
(C, D) Visual function of both, rods and cones, was compromised after injection of intermediate and high $NaIO_3$ dosages, as shown by the amplitudes of the scotopic (C, 0.003 cd*s*m-2) and photopic (D, 10 cd*s*m-2) b-waves over time.
(E, F) DAPI staining and DIC imaging at 7 days after injection shows a normal RPE (arrows) and neuroretinal phenotype in the control group (E, saline injection). The RPE in animals injected with 30 mg/kg bw $NaIO_3$ (F) is no longer a continuous monolayer, but patchy and unorganized (arrows).
(G) Injection of 30 mg/kg bw $NaIO_3$-injection causes the development of highly reflective speckles in the previously homogenous fundus image. Fluorescein angiography (FA) further shows the change in blood-retina barrier permeability as a result of the $NaIO_3$-injection, with the fluorescein-bright inner plexus vessels clearly standing out from the dark retina initially. At 7 days post $NaIO_3$ injection, the contrast is strongly reduced due to fluorescein leakage through the destroyed RPE layer.
Scale bars: 50 µm (E,F). cho, choroid; onl, outer nuclear layer; FA, fluorescein angiography.

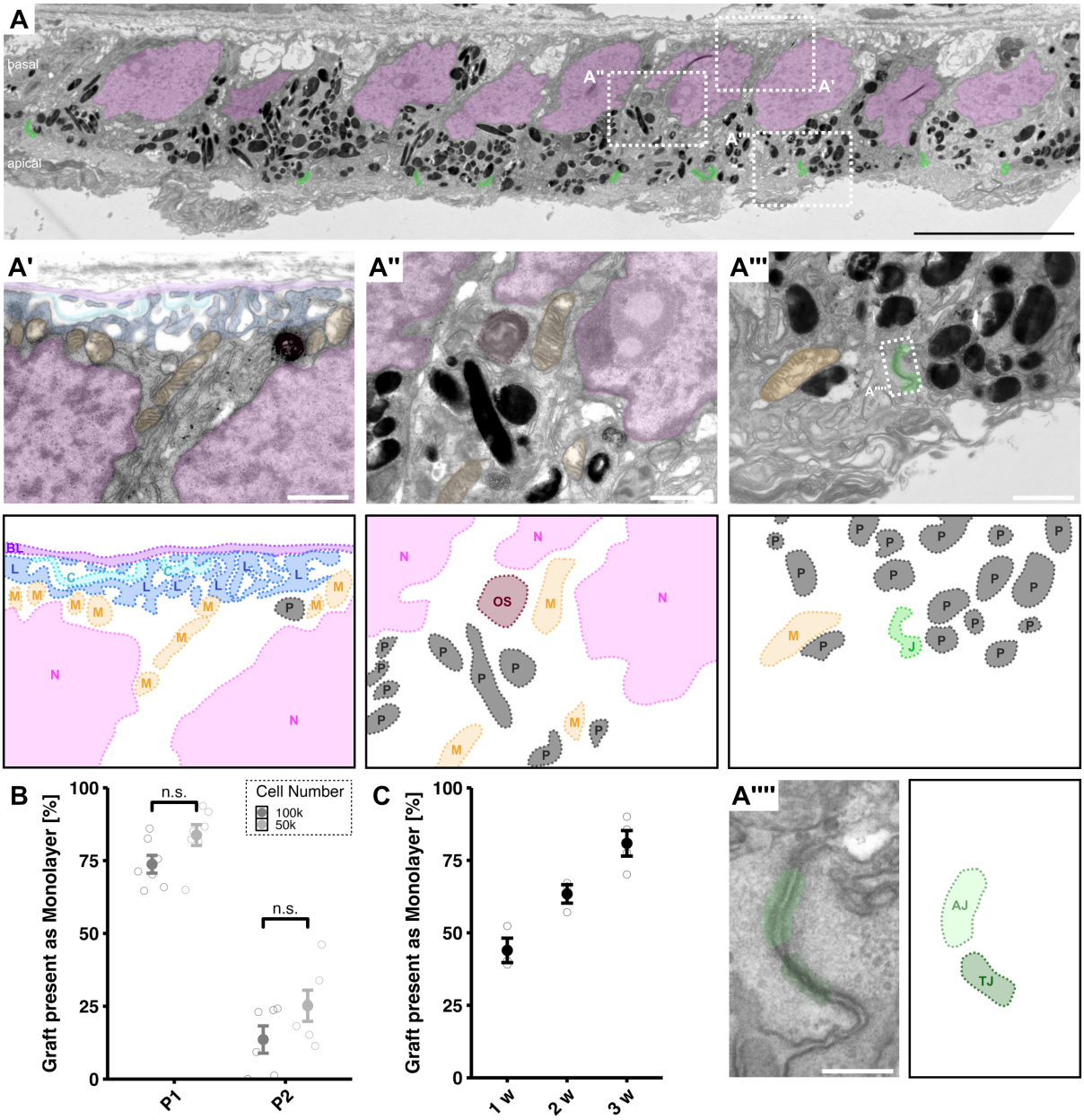

Figure S2: RPE-derived monolayer formation and characterisation

(A) Transmission electron microcopy (TEM) image presented in figure 2E with higher magnifications showing a basal (A’), an intermediate (A’’) and an apical (A’’’) portion of the cells with RPE-characteristic features. Apical junctions are further highlighted per green overlay in A and one junctional complex from A’’’ is magnified in A’’’’. TEM images A’-A’’’’ are depicted with coloured overlays, with the labelled overlay additionally positioned next to the respective image for better visibility.

(B) Monolayer percentage data presented in figure 2G, replotted to show differences between eyes having obtained 50,000 or 100,000 cells. While the difference is not statistically significant (t-test), transplantation of 50,000 cells tends to generate a higher monolayer percentage than transplantation of 100,000 cells.

(C) Monolayer percentage increases over time. Here, empty points represent graft quantification of a single central section.

Scale bars: 10 µm (A), 1 µm (A’-A’’’), 200 nm (A’’’’). AJ, adherens junctions; BL, basal lamina; C, collagen; J, junctional complexes; L, basal labyrinth; M, mitochondrium; N, nucleus; OS, phagocytosed outer segment; P, pigment granule; TJ, tight junctions; w, weeks.

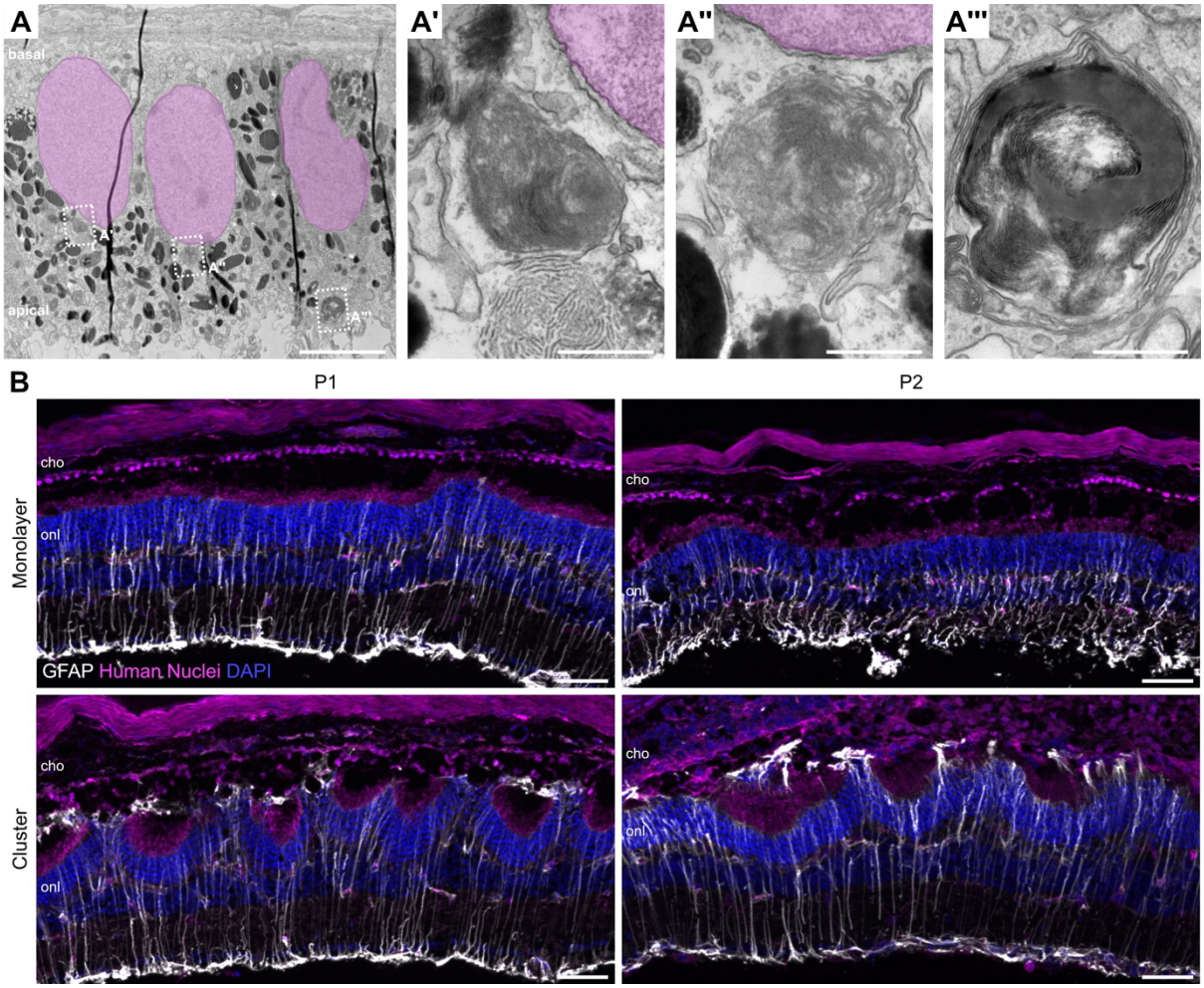

Figure S3: Supplementary data for Figure 3.
(A) Transmission electron microcopy images of RPE-derived monolayers show outer segment particles within transplanted cells. A'-A''' show boxed areas in A magnified.
(B) GFAP staining found throughout all neuroretinal layers shows reactive Müller Glia irrespective of RPE passage transplanted or graft cell conformation as monolayer or cluster.
Scale bars: 50 µm (B), 5 µm (A) and 500 nm (A'-A'''). cho, choroid; onl, outer nuclear layer.

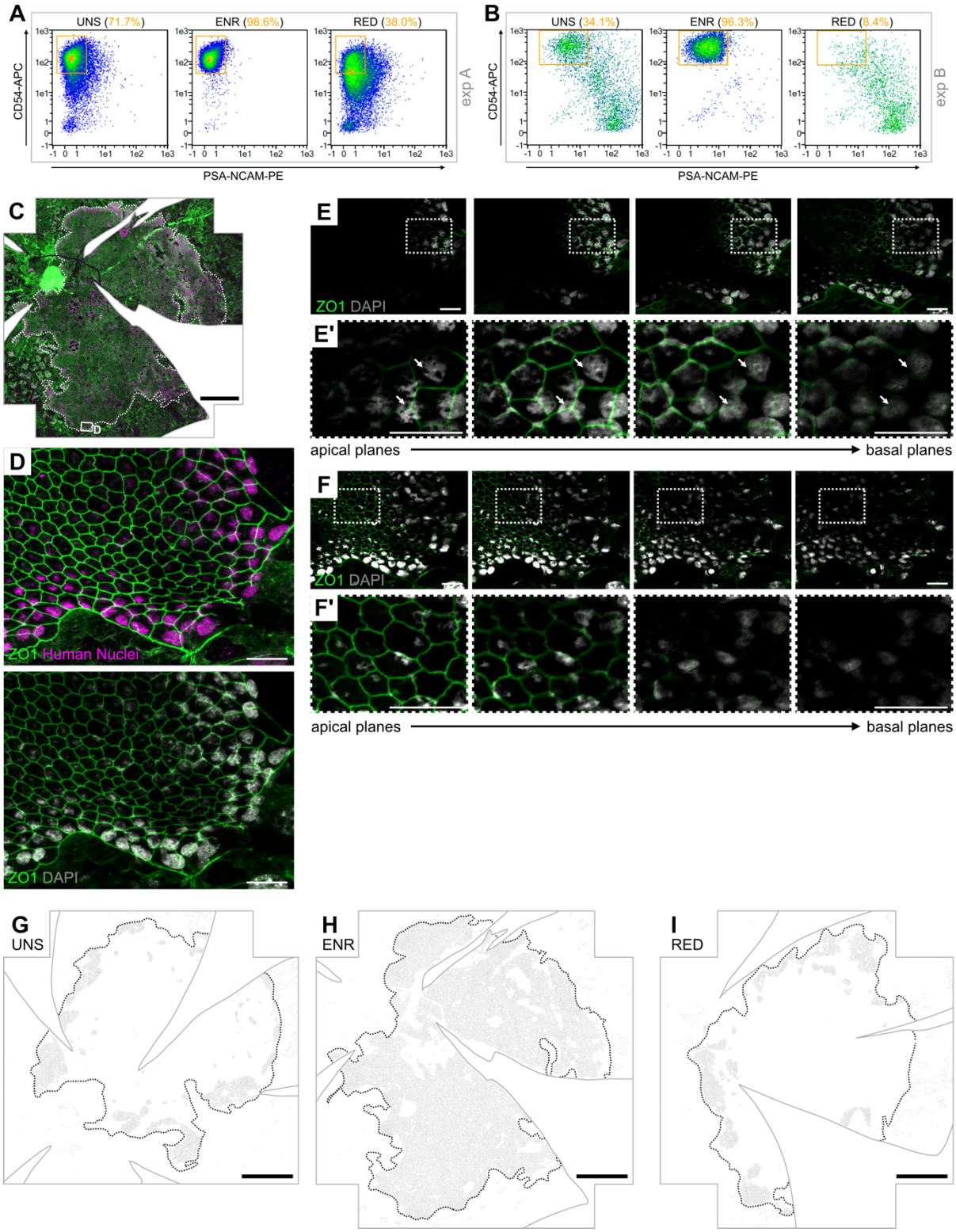

Figure S4: Supplementary data for Figure 5.

(A, B) Flow cytometry re-analysis of unsorted (UNS), CD54^{+}/PSA-NCAM^{-}-enriched (ENR) and -reduced (RED) fractions before transplantation in experiment A (exp A, see also figure 5I) and experiment B (exp B, see also figure 5J). Orange numbers show purity of the target cell population in each fraction, with a high percentage of CD54^{+}/PSA-NCAM^{-} cells in exp A (71.7%) and a lower percentage of CD54^{+}/PSA-NCAM^{-} cells in exp B (34.1%).

1037 (C) Flatmount of the ENR graft as presented in figure 5B, here with an additional region framed and magnified
1038 in D-F'.
1039 (D) Immunohistochemistry shows higher visibility of the Human Nuclei and DAPI staining towards the edge of
1040 the human graft.
1041 (E, F) Single z-planes of the maximum intensity projection in D, with E' and F' showing the boxed regions in E and
1042 F enlarged, highlighting the obstruction of nucleus visibility through the apically located pigment
1043 (arrows). DAPI brightness is increased in F and F' for better visibility.
1044 (G-I) REShAPE cell outlines of the flatmounted eyecups shown in figures 5A-C, with human graft areas denoted
1045 by dotted lines. Eyes received transplantations of cell suspensions that were either unsorted (G), enriched
1046 (H), or reduced (I) in $CD54^{+}$/PSA-$NCAM^{-}$ cells.
1047 Scale bars: 500 µm (C, G-I), 20 µm (D-F').

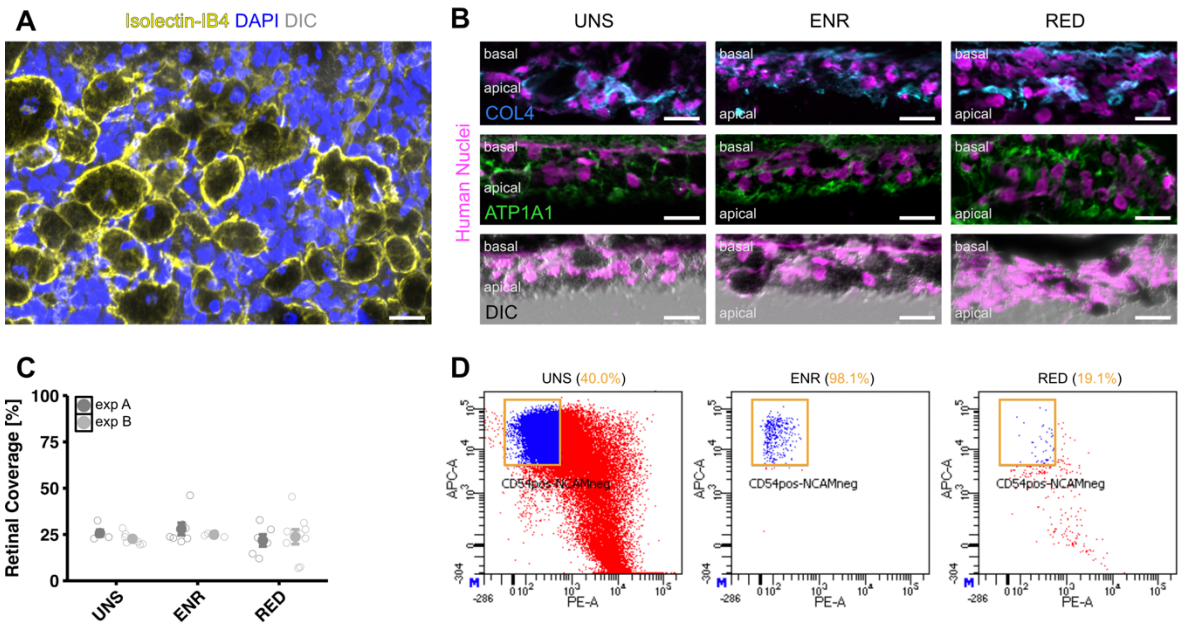

Figure S5: Supplementary data for Figure 5, continued.

(A) Pigmented, spherical clumps likely represent macrophages as they are larger than the average RPE cells, contain a single nucleus and stain positive for isolectin IB_4. Here, pigmented clumps are shown stained on top of the outer nuclear layer of a retinal flatmount opposing an unsorted human RPE graft.

(B) Clusters formed by all graft fractions lack polarization, as basal marker COL4 and the apical marker ATP1A1 are expressed chaotically throughout the cluster. Similarly, the pigment (dark in DIC images) is not confined to the apical cytosol but mostly situated throughout the cluster.

(C) Quantification of retinal coverage after transplantation of RPE cells from experiments A and B (exp A and exp B, representing the experiments depicted in figures 5I and 5J, respectively) shows a similar coverage in all fractions, irrespective of $CD54^+$/PSA-$NCAM^-$ cell purity.

(D) Reanalysis of the unsorted (UNS), $CD54^+$/PSA-$NCAM^-$-enriched (ENR) and -reduced (RED) fractions of RPE sorted with an Aria III flow cytometer. Orange boxes show the target cell sorting gate and orange numbers show purity of the target cell population per fraction.

Scale bars: 20 µm (A, B).